A review of mechanisms generating seismic anisotropy in the upper mantle

Lars N. Hansen[1], Manuele Faccenda[2], and Jessica M. Warren[3]

[1]Dept. of Earth and Environmental Sciences, University of Minnesota, Minneapolis, MN 55455, USA

[2]Dept. of Geoscience, University of Padua, 35131, Padua, Italy

[3]Dept. of Earth Sciences, University of Delaware, Newark, DE 19716, USA

Abstract

Seismic anisotropy is a key observational tool for mapping flow in Earth's upper mantle. However, interpreting patterns of anisotropy relies on a firm understanding of the microphysical mechanisms that generate anisotropy. Here we discuss our current understanding of the generation of intrinsic and extrinsic seismic anisotropy in upper-mantle rocks. Intrinsic anisotropy results from the elastic anisotropy of the constituent minerals. We address the role of thermochemical conditions in modifying the manner in which these minerals align with the deformation reference frame, controlling the macroscopic anisotropy. Extrinsic anisotropy results from the composite behavior of a material composed of multiple phases. We examine the influence of mineralogical layering and the presence of a melt phase on anisotropy, including the interaction between extrinsic and intrinsic anisotropy. Finally, we compare and contrast existing methods to forward model the development of anisotropy in the upper mantle and demonstrate that current predictions suggest most observed anisotropy results from intrinsic anisotropy when fluids are not present.

1 Introduction

Mapping the patterns of flow in Earth's convecting mantle is an essential component of understanding the dynamics and evolution of our planet. Without the option for direct observation, we must turn to indirect means for inferring flow. Perhaps the most successful endeavour in this regard has been observations of anisotropy in the seismic properties of the upper mantle. That is, seismic wave speeds

can vary as a function of their propagation and/or polarization directions (e.g., Crampin, 1981).

In a critical early contribution, Hess (1964) recognized that P-waves propagating parallel to fracture zones in the eastern Pacific were faster than those propagating perpendicular to fracture zones. From this observation he recognized a correlation between seismic anisotropy and tectonic processes in the upper mantle. This key insight opened the possibility of mapping patterns of mantle convection using seismological techniques. Subsequent efforts aimed to use global maps of anisotropy in polarization direction (Nataf et al., 1984) or propagation direction (Tanimoto and Anderson, 1984) to interpret large-scale flow patterns, leading to a variety of new insights into upper mantle dynamics. A wide range of global (e.g., Beghein et al., 2014; Chang et al., 2015; French and Romanowicz, 2014; Moulik and Ekström, 2014; Schaeffer and Lebedev, 2013) and regional (e.g., Fichtner et al., 2010; Gaherty et al., 1996; Nishimura and Forsyth, 1989; Russell et al., 2019; Yuan and Romanowicz, 2010) tomographic models including anisotropy are now available. Many of these models have been demonstrated to agree well with simulations of mantle convection (Becker et al., 2014, 2006). Besides tomographic models, seismic anisotropy is frequently detected by the splitting of core-refracted shear waves (SKS, SKKS), which have a much better lateral resolution than surface waves, but are lacking in vertical resolution. Nevertheless, these teleseismic phases are demonstrated to be mostly sensitive to the anisotropy at upper mantle depths (Sieminski et al., 2008). As such, they provide important information about fabrics and their relation to flow patterns within this part of the mantle (e.g., Eakin et al., 2018; Long and Silver, 2008; Silver, 1996; Wolfe and Solomon, 1998).

Although much progress has been made in understanding mantle dynamics from seismic anisotropy, most of this work relies on assumptions about the physical origin of that anisotropy. Seismic anisotropy results from anisotropy in a medium's elastic properties. Considering the typical wavelengths of teleseismic waves (>5 km), seismic anisotropy is essentially an average of the anisotropy of features smaller than those wavelengths, including features at the grain scale (microns to millimeters) and the outcrop scale (meters to kilometers). As illustrated in Figure 1a, crystals of all

minerals are inherently anisotropic in their elastic properties, and crystallographic alignment of many crystals in an aggregate can lead to a material that is macroscopically anisotropic, a phenomenon referred to as *intrinsic* anisotropy. The manner in which those crystals align depends on a wide range of physical and chemical variables. Additionally, as illustrated in Figure 1b, layering (or other non-random arrangements) of different materials can lead to macroscopic anisotropy, which is referred to as *extrinsic* anisotropy. The layered materials can be anything with contrasting elastic properties such as combinations of different minerals or liquids.

Observations of seismic anisotropy are therefore often linked to thermochemical conditions and the history of mantle processes. These links are extremely useful for understanding modern geodynamic systems, testing geodynamic hypotheses, and benchmarking geodynamic simulations. However, interpretations must also be made carefully, as the geometric relationships between seismic anisotropy and large-scale mantle processes can change dramatically depending on the mechanism leading to anisotropy and the ambient physical and chemical conditions, some of which are not yet fully understood (e.g., Bernard et al., 2019; Hansen et al., 2014; Jung and Karato S, 2001; Mainprice et al., 2005). Here we review the common mechanisms for generating anisotropy in upper mantle rocks, describe their implementation into geodynamic simulations, and discuss first-order predictions of the distribution of anisotropy in the upper mantle.

2 Definitions of anisotropy

The terminology used to describe anisotropy is varied and may often differ between mineral physicists and seismologists. Several reviews have recently outlined the nomenclature and physical meaning of different descriptors of anisotropy (Almqvist and Mainprice, 2017; Long and Becker, 2010; Mainprice, 2007; Skemer and Hansen, 2016) and we only briefly introduce the key terminology here.

The seismic anisotropy of an elastic medium can be described both in terms of P-waves and in terms of S-waves. In general, P-wave anisotropy is a description of the variation in the P-wave velocity, V_P, as a function of the propagation direction and is often reported as a percentage deviation from the

average V_P. S-waves entering an anisotropic medium are decomposed into two orthogonally polarized S-waves with different velocities. The S-wave anisotropy is generally described by either the difference in velocity between the slow and fast S-waves, ΔV_S, or by the polarization direction of the fast wave. A full description of P-wave and S-wave anisotropy can be calculated for any elastic medium if all components of the elastic stiffness tensor, C_{ijkl}, of the medium are known (21 independent values for the most general case). In that case, one can calculate the Christoffel tensor,

$$T_{ik} = C_{ijkl} d_j d_l, \tag{1}$$

where d is the direction of wave propagation (for a review, see Mainprice, 2007). The key wave velocities are then given by

$$V_{\mathrm{p}} = \sqrt{\frac{\lambda_1}{\rho}}, \quad V_{\mathrm{s1}} = \sqrt{\frac{\lambda_2}{\rho}}, \quad \text{and} \quad V_{\mathrm{s2}} = \sqrt{\frac{\lambda_3}{\rho}}, \tag{2}$$

where λ_1, λ_2, and λ_3 are the eigenvalues of T_{ik} and ρ is the density. V_{s1} and V_{s2} are the fast and slow S-wave polarizations, respectively, and their difference is ΔV_S. The eigenvectors of T_{ik} represent the polarization directions of the three waves, respectively.

The elastic properties of geological materials often exhibit symmetry that reduces the number of independent values of the stiffness tensor. Two key examples are orthorhombic symmetry, found in olivine and orthopyroxene, and hexagonal symmetry (also referred to as transverse isotropy)[1], found in the high-pressure phase of iron. In the former, three distinct and orthogonal directions describe the maximum, intermediate, and minimum directions of anisotropy. In the latter, a single plane exists in which the medium appears isotropic, while the direction normal to that plane exhibits significantly different properties. General anisotropy can be decomposed into stiffness tensors with these higher symmetries (Browaeys and Chevrot, 2004), allowing the overall symmetry of the elastic properties to be assessed.

Due to the nature of tomographic inversions of seismic data, complete characterization of all elements

[1] For further insight into the form of the stiffness tensor for a given symmetry, see Appendix E in Nye (1985).

of the stiffness tensor is generally not feasible. Therefore, the anisotropy is often assumed to be of reasonably high symmetry and in a favorable orientation to reduce the necessary number of parameters for its description. A common descriptor of anisotropy observed in Earth is the radial anisotropy, ξ, which is defined as the squared ratio of the horizontally polarized S-wave velocity to the

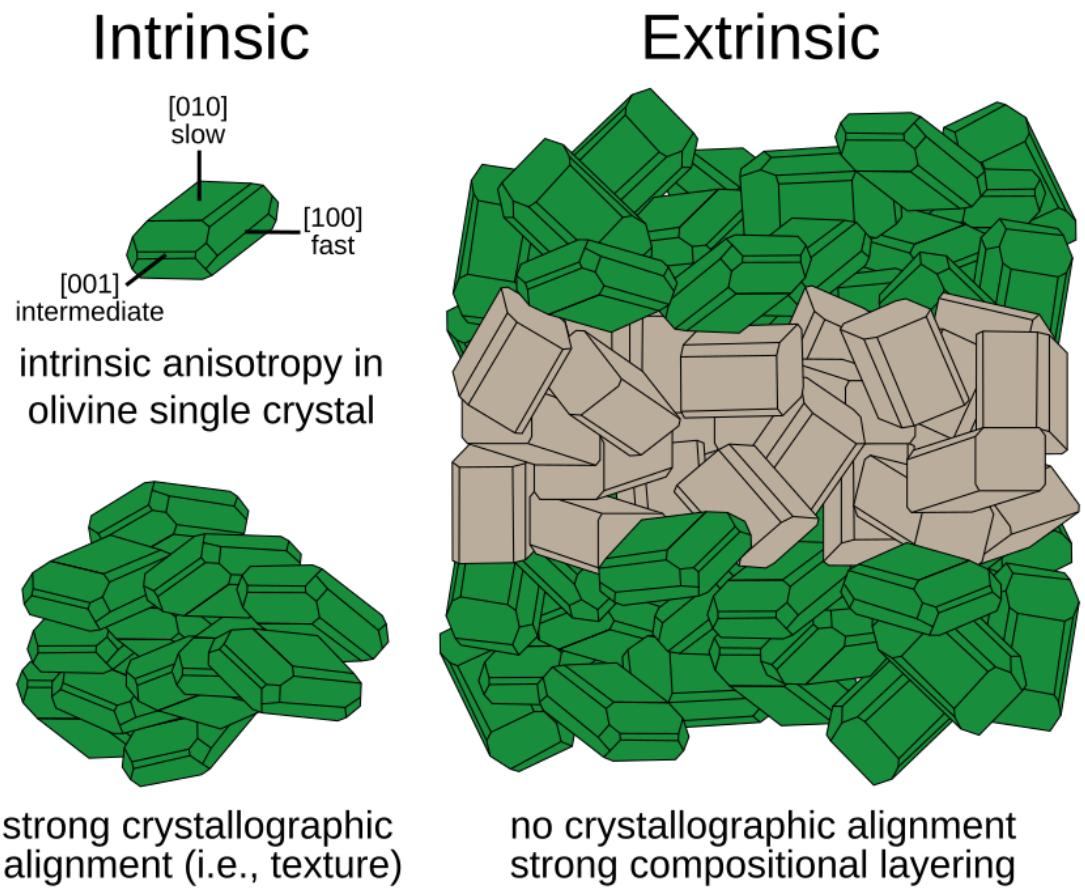

Figure 1: Schematic illustration of intrinsic and extrinsic anisotropy. Intrinsic anisotropy results from the crystallographic alignment of crystals that are inherently anisotropic. Extrinsic anisotropy results from the heterogeneous spatial distribution of multiple phases (e.g., compositional layering).

vertically polarized S-wave velocity, $\left(\frac{V_{SH}}{V_{SV}}\right)^2$. This description of anisotropy effectively assumes that the stiffness tensor has transverse isotropy with the axis of symmetry normal to Earth's surface. Transverse isotropy can also be described with the Love parameters[2] (*A*, *C*, *F*, *L*, *N*), for which *A* and

[2] See also the relationship between the Love parameters and the Thomsen parameters (e.g., Mainprice, 2007)

C relate to the P-wave anisotropy and L and N relate to the S-wave anisotropy ($\xi = N/L$). The Love parameters were expanded for more general anisotropy by Montagner and Nataf (1986). Departures from radial anisotropy can be described by the azimuthal anisotropy, which is based on changes in wave speed for different propagation or polarization directions within the plane parallel to Earth's surface. Based on the expansion by Montagner and Nataf (1986), magnitudes of azimuthal anisotropy, G, are often reported as a percentage of the parameter L.

3 Generation of anisotropy

Interpreting seismological observations of the magnitude, orientation, and symmetry of anisotropy, or forward modelling their evolution, requires an intimate understanding of the physical mechanisms leading to that anisotropy. A wide range of physical processes contribute to generating anisotropy in rocks, and here we describe the primary processes relevant to anisotropy in Earth's upper mantle.

3.1 Intrinsic anisotropy

All minerals are inherently anisotropic in their physical properties. As an extreme example, if grains within an aggregate all share the same crystallographic orientation (i.e., they have a single crystallographic preferred orientation, or CPO), then the aggregate will exhibit macroscopic anisotropy identical to that of a single crystal. In a more typical example, grain orientations may not be exactly the same, but grains with certain orientations have a higher probability of occurring (i.e., the orientation distribution is non-uniform), in which case some anisotropy will still be imparted to the macroscopic aggregate. In general, we refer to these aggregates as *textured*, which is a more general term that also refers to aggregates with multiple, high-probability crystallographic preferred orientations.

Precise calculation of the elasticity of an aggregate of anisotropic grains is nontrivial, particularly because of the local requirements to maintain strain compatibility and stress equilibrium. Recent reviews of this topic have been provided by Almqvuist and Mainprice (2017) and Skemer and Hansen

(2016). The most robust methods currently available involve explicitly discretizing the microstructural arrangement of grains and solving for the stress and strain fields using the finite-element method (e.g., Zhong et al., 2014) or a Fourier-transform-based approach (e.g., Brenner et al., 2009). These computationally expensive techniques can be used to benchmark simplified averaging schemes, such as the Voigt and Reuss bounds, which assume every grain is subject to the same strain or the same stress, respectively, or the Hill average, which takes the arithmetic mean of the stiffness tensors predicted by the Voigt and Reuss bounds. Of these simplified averages, the Voigt average is commonly used in the geosciences since it best approximates the magnitude of anisotropy in the aggregate (Crosson and Lin, 1971; Peselnick et al., 1974; Zhong et al., 2014).

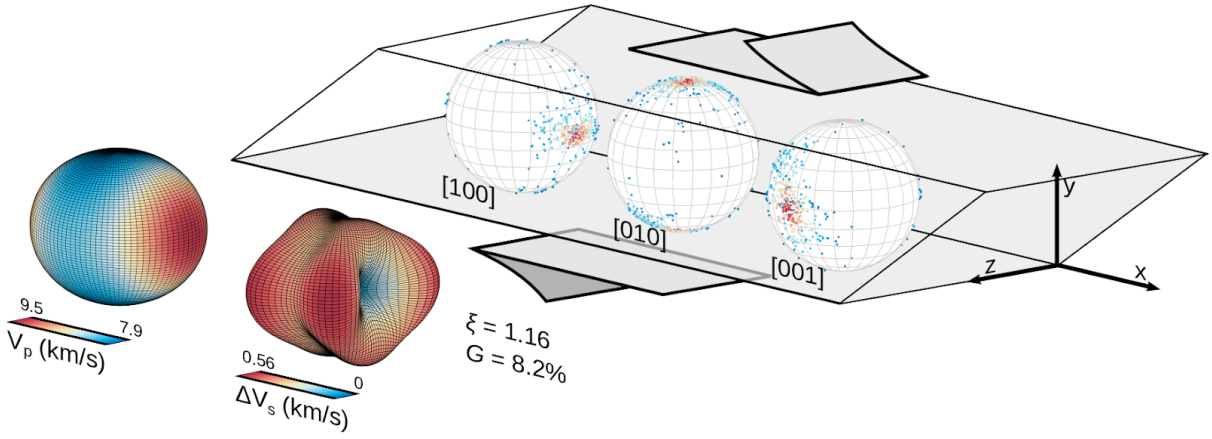

Figure 2: Demonstration of intrinsic seismic anisotropy generated from a typical CPO in an experimentally sheared olivine aggregate (sample PT0651 from Hansen et al. (2012a)). The shear direction is parallel to *x*. 3-D diagrams are given for crystallographic orientation distributions, the directional dependence of P-wave velocities, and the directional dependence on the difference in S-wave velocity between the two s-wave polarizations. Values are reported for the magnitude of radial anisotropy, ξ, and the magnitude of azimuthal anisotropy, *G*, as a percentage of *L*. 3-D projections were generated with the MTEX toolbox for Matlab® (Mainprice et al., 2011).

Figure 2 presents an example of the macroscopic elastic seismic properties calculated from a distribution of orientations of olivine crystals in an experimentally deformed peridotite using the Voigt

average. This particular sample exhibits strong alignment of [100], with moderate alignment of [010] and [001]. The V_p and ΔV_s anisotropies are dominated by the [100] alignment, leading to an aggregate anisotropy with nearly hexagonal symmetry, even though a single crystal of olivine has orthorhombic symmetry. Because intrinsic anisotropy arises from crystal orientation distributions, mechanisms for producing anisotropic aggregates inherently involve grain rotations. Importantly, those grain rotations need to be linked somehow to the crystallography. The two primary mechanisms for grain rotation linked to crystallographic orientations are crystal-plastic deformation and rigid rotation of elongate grains whose shape is crystallographically controlled.

3.1.1 Grain rotations controlled by crystal-plastic dislocation motion

Crystal plastic deformation inherently involves the motion of lattice dislocations. Dislocations are line defects in a crystal whose motion results in a shear strain of the lattice (for a recent review, see Kohlstedt and Hansen, 2015 and references therein)(for a recent review, see Kohlstedt and Hansen, 2015). This can be visualized as a lattice plane along which shearing occurs (the slip plane), whose normal vector is **n**. Slip only occurs in the slip direction, which is defined by the Burgers vector, **b**. The two vectors **n** and **b** define a slip system. The slip system can only operate if a shear stress is applied on the slip plane in the direction of the burgers vector. For arbitrary stress states, the resolved shear stress describes the magnitude of the stress acting on the slip plane in the slip direction. The Schmid tensor is defined as,

$$M_{ij} = \tfrac{1}{2}(b_i n_j + b_j n_i), \tag{3}$$

and provides a framework for determining the resolved shear stress, τ, according to $\tau = M_{ij}\sigma_{ij}$, where **σ** is the deviatoric stress tensor. The motion of dislocations in their slip plane (i.e., glide) produces a shear strain in the reference frame of the slip system at a given strain rate, $\dot{\gamma}$, that is related to the full strain rate tensor according to $\dot{\varepsilon}_{ij} = M_{ij}\dot{\gamma}$.

In addition to strain, the glide of dislocations also produces a rotation, defined as

$$Q_{ij} = \frac{1}{2}(b_i n_j - b_j n_i), \quad (4)$$

where the rotation tensor, **Q**, defines a rotation about the axis **n**×**b**. Hence, the rotation of crystals due to dislocation glide is inherently linked to the crystallographic directions **n** and **b**.

Crystalline materials generally have more than one slip system available. However, for the same magnitude of resolved shear stress, different slip systems will produce different strain rates due to differences in the ease of dislocation motion on different glide planes. Importantly, the rate of rotation is given by $Q_{ij}\dot{\gamma}$. Therefore, slip systems that generate faster strain rates (often referred to as "easy" slip systems) contribute more to the rotation of a grain than do slip systems that generate slower strain rates (often referred to as "hard" slip systems). In some minerals, such as mica, the difference in strength between easy and hard slip systems is so great that the deformation and microstructural evolution is effectively dominated by a single slip system. Therefore, certain mineral systems cannot accommodate an arbitrary deformation if fewer than five linearly independent slip systems are available, as pointed out by von Mises (1928).

For olivine, the (010)[100] slip system (where round brackets denote **n** and square brackets denote **b**) is the easiest over a wide range of conditions (Figure 3a). It has been demonstrated experimentally (Bystricky et al., 2000; Hansen et al., 2014; Zhang et al., 2000; Zhang and Karato, 1995) and computationally (Hansen et al., 2016a; Kaminski and Ribe, 2001; Ribe and Yu, 1991; Tommasi et al., 2000) that the easy slip system controls the first-order characteristics of the CPO produced during crystal plastic deformation. The key feature of these CPOs is the preferred alignment of the [100] axis of olivine with the shear direction (e.g., Figure 2), which primarily occurs in simulations if the (010)[100] slip system is the easiest slip system. Experimentally, this link between slip system and CPO is assessed by comparing experiments on single crystals to experiments on aggregates of grains. Figure 3 depicts the results of a series of single-crystal experiments from Bai et al. (1991).

The correspondence between the predicted weak (010)[100] slip system and observed CPOs with [100] aligned with the shear direction suggests that transitions in CPOs as a function of

thermomechanical conditions can be predicted from single crystal flow laws. The flow laws for olivine (Figure 3) reveal the relative strength of different slip systems as a function of stress, temperature, oxygen fugacity, silica activity, and confining pressure. All slip systems are observed to have the same stress dependence, so a transition is not observed as a function of stress. All other parameters, however, do lead to transitions in the easiest slip system, however relatively few of these parameters have been investigated, as described below. In the discussion that follows, we discuss the controls on changes in slip systems in olivine in order of most to least constrained.

3.1.1.1 Slip system strength as a function of temperature

Different activation energies for the various slip systems leads to transitions in the easiest slip system as a function of temperature (Figure 3b). Although the experiments of Bai et al. (1991) were constrained to relatively high temperatures (>1200°C), Carter and AvéLallement (1970) demonstrated transitions in the easiest slip system at lower temperatures in experiments extending down to~600°C. In addition, based on a compilation of data, Goetze (1978) suggested that transitions occur in the easy slip system as a function of temperature. Unfortunately, because of the necessary increase in differential stress (and often confining pressure) to maintain laboratory strain rates at lower temperatures, the impact of temperature on CPO has not been rigorously deconvolved from other effects.

3.1.1.2 Slip system strength as a function of oxygen fugacity

Oxygen fugacity also affects the relative strength of different slip systems (Figure 3c). The primary role of oxygen fugacity in moderating creep strength is through its influence on point defect concentrations and therefore on the chemical diffusion that limits the dislocation climb velocity (e.g., Kohlstedt and Hansen, n.d.). As evidenced by the crossing of the solid blue and dashed back lines in Figure 3c, the most obvious transition in relative slip system strength occurs at less than two log units below the Ni:NiO buffer. This critical oxygen fugacity is within the range of oxygen fugacities in the upper mantle inferred from basalt chemistry (e.g., Cottrell and Kelley, 2011). However, at low

223

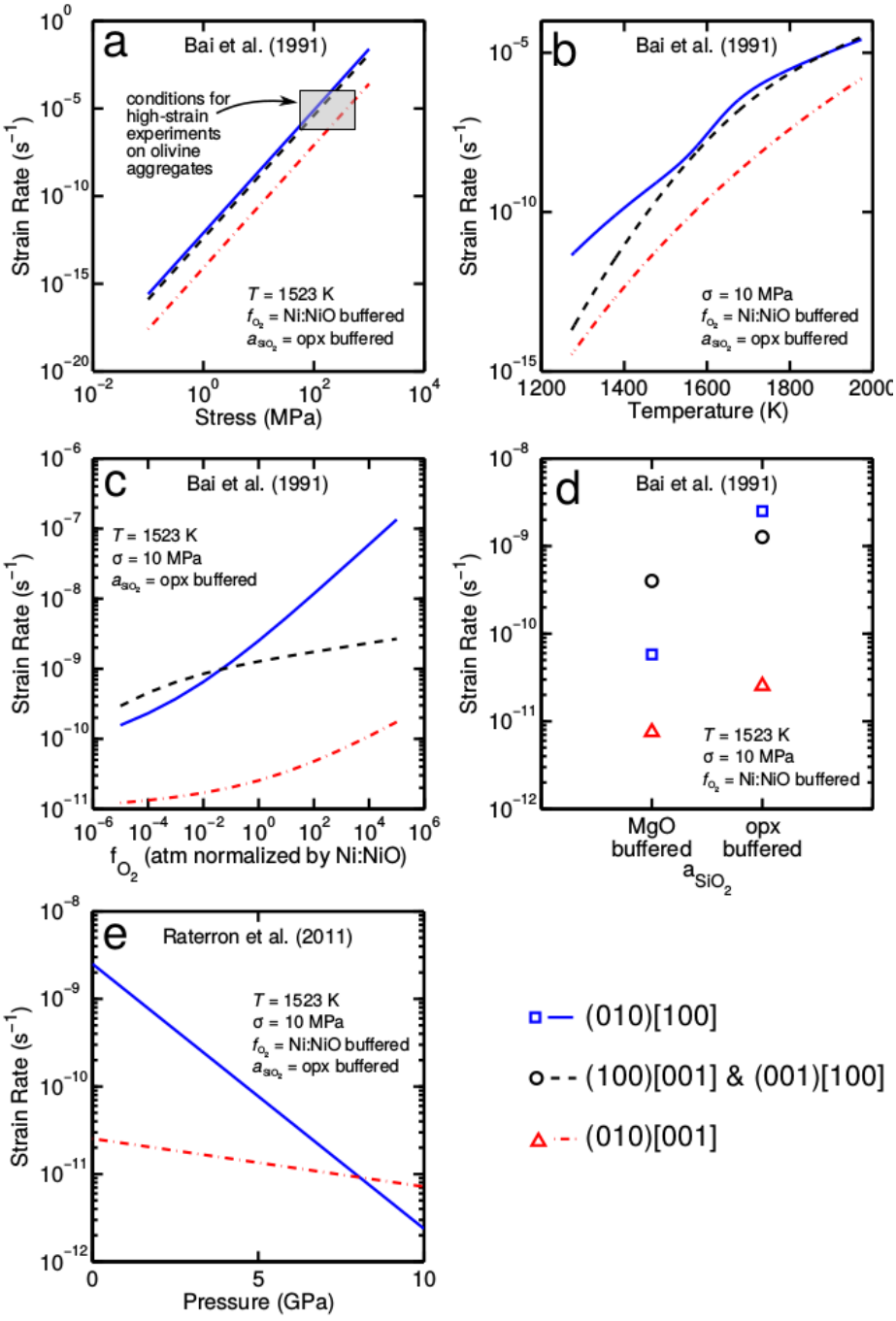

224 Figure 3: Predictions of strain rates in olivine single crystals as a function of (a) stress, (b)
225 temperature, (c) oxygen fugacity, (d) silica activity, and (e) confining pressure. Strain rates are
226 calculated using the flow laws from Bai et al. (1991) and Raterron et al. (2011). For each plot, the
227 strain rate is indicated as a function of one independent variable, and all other variables are held
228 constant as indicated.

fugacities in Figure 3c, whether (001)[100] or (100)[001] will dominate is unclear because these slip systems could not be distinguished in the original experiments. Therefore the predicted effect on CPO evolution is uncertain, and the impact of oxygen fugacity on CPO remains a target for future investigation. The closest approach so far comes from Keefner et al. (2011), who examined CPOs in dunites deformed at two very different oxygen fugacities. Unfortunately, the low strains in those experiments and a pre-existing CPO in the starting material make it difficult to isolate any role of oxygen fugacity in modifying the CPO.

3.1.1.3 Slip system strength as a function of silica activity

The silica activity of a system also modifies point defect concentrations and therefore can influence the strain rate. Figure 3d demonstrates that the relative strengths of olivine slip systems depends on the silica buffer. As with oxygen fugacity, the role of silica activity in modifying CPO has not been explored. A transition in CPO might be induced by buffering the silica activity with a silica-poor phase like MgO, but it currently seems unlikely that significant portions of the upper mantle have such low silica activity (e.g., Salters and Stracke, 2004).

3.1.1.4 Slip system strength as a function of pressure

The confining pressure may also influence the relative strengths of different slip systems in olivine. Experiments on forsterite single crystals presented by Raterron et al. (2012, 2011, 2009, 2007) and illustrated in Figure 3e suggest that a slip system with a [001] Burgers vector becomes easiest at confining pressures above ~8 GPa at a temperature of 1523 K (note that Table 4 in Raterron et al. (2012) includes a typo, and flow laws for $[011]_c$ should be in series rather than in parallel). This transition in slip system strength is predicted to move to lower pressures with increased temperature. Pressure-induced transitions in olivine CPO have been observed in several experiments on dry olivine aggregates (Jung et al., 2009; Ohuchi et al., 2011).

Karato et al. (2008) suggested that care must be taken when examining CPO transitions as a function of confining pressure as most high-pressure experiments are also characterized by high differential

stresses. These high stresses would likely cause a transition from dislocation creep to low-temperature plasticity (Goetze and Poirier, 1978). Under dry conditions, low-temperature plasticity appears to primarily involve [001] dislocations (Carter and Ave'lallemant, 1970; Gaboriaud et al., 1981) Therefore high-pressure experiments producing CPOs with [001] aligned with the shear direction may result from high differential stresses rather than high confining pressures. However, Raterron et al. (2012) subsequently argued that, although involving high differential stresses, many experiments with evidence for high activity of slip systems with [001] Burgers vectors still appear to be dominated by dislocation creep when data are compared to published deformation mechanism maps for olivine (Frost and Ashby, 1982, Chapter 15). Comparison of mechanical data from high-pressure experiments to more recently published deformation mechanism maps (e.g., Hansen et al., 2011) confirms the argument of Raterron et al. (2012), with only the data points collected at the highest stresses plotting in the low-temperature plasticity regime. There is still scope, however, for confirming that a pressure-induced transition in CPO occurs at lower differential stresses (<300 MPa).

3.1.1.5 Slip system strength as a function of water fugacity

The water concentration or water fugacity of a system is also of major importance to olivine deformation. Water fugacity influences point defect concentrations in olivine (e.g., Kohlstedt, 2006), significantly impacting rates of dislocation creep. The effect of water on the relative strengths of different slip systems is *not* depicted in Figure 3 because insufficient flow laws have been published for olivine single crystals deformed under wet conditions. Flow laws exist for the (010)[100] slip system (Girard et al., 3/2013) and the (100)[001] and (001)[100] slip systems (Tielke et al., 2017) under wet conditions. However, a complete assessment of the role of water in transitions in the easy slip system requires a flow law for the (010)[001] slip system and, ideally, all three flow laws would be calibrated in the same set of experiments to rule out systematic bias between experimental protocols. We note that all these slip systems were also investigated under hydrous conditions in the experiments of Mackwell et al. (1985), however the relatively low confining pressures of those

experiments necessarily involved relatively low water fugacities, and a transition in the easiest slip system was not observed.

Although water-induced transitions in slip system strength have not been rigorously demonstrated, a variety of experimental studies on aggregates of olivine have documented transitions in CPO associated with different combinations of water concentration, temperature, and differential stress (Jung et al., 2006; Jung and Karato S, 2001; Katayama et al., 2004). These results suggest that the incorporation of dissociated water into the olivine lattice can lead to distinct differences in the crystallographic axes that align with the shear direction. The systematics and mechanisms behind these water-induced transitions in CPO were reviewed by *Karato et al.* (2008). However, a demonstrable link between olivine CPO and the behavior of olivine single crystals under wet conditions remains a clear target for future research.

Recent studies of naturally deformed peridotites have looked for evidence of a relationship between CPO and water content. Based on analysis of water in four samples from shear zones in the Josephine Peridotite, Skemer et al. (2013) concluded that CPO varies as a function of water content. However, Kumamoto et al. (2019) found that CPO type does not vary systematically as a function of olivine water content. Bernard and Behr (2017) found that, in xenoliths from the Mojave lithospheric mantle, olivine CPO does not correlate with water content, while Bernard et al. (2019) reached the same conclusion in a survey of global xenoliths. All of these studies have also found that CPO does not vary systematically with strain or stress, suggesting that the kinematics of deformation may be the controlling factor in the type of CPO that develops. However, further studies of peridotites in settings where deformation conditions can be constrained are needed to elucidate the variables controlling olivine CPO.

3.1.1.6 Mechanisms for changes in slip system strength

The mechanisms behind changes in the relative strengths of slip systems as a function of the physical and chemical conditions that control dislocation motion are not yet clear. In olivine, the dislocation

glide velocity, and therefore the induced grain-rotation rate, during dislocation creep is generally thought to be limited by the dislocation climb velocity (e.g., Kohlstedt, 2006). That is, discrete obstacles (e.g., dislocation dipoles) act to impede dislocation glide, and those obstacles are overcome (or they are removed) by dislocation climb, which is relatively slow. The specific relationship between the climb velocity and the macroscopic relationship is complex, and requires knowledge of the details of the dislocation arrangement. Useful examples of this complexity in olivine are presented in the discrete-dislocation dynamics simulations of Boioli et al. (2015) and Gouriet et al. (2019). Dislocation climb is a non-conservative, diffusion-limited process, and therefore anything that influences diffusion rates (e.g., point-defect concentrations) will influence the overall creep rate. However, for changes in the relative velocities of different types of dislocations to occur, changes in the physical and chemical conditions must modify the climb velocities of some dislocations more than others.

For water, Karato et al. (2008) proposed that the density of jogs (defects essential to climb that locally displace the dislocation line onto a neighboring slip plane) or kinks (defects essential to glide that locally displace the dislocation line within the slip plane) is modified in an anisotropic manner by the water content. Whether this effect is directly due to OH^- defects or to modifications in the concentrations of other point defects is not clear. Furthermore, whether this same mechanism can be responsible for transitions due to temperature, pressure, and silica activity is unclear. Future research into the role of each physical and chemical parameter in modifying kink and jog densities is needed.

Another potential solution is that dislocation velocities in dislocation creep are limited by another mechanism entirely. For example, Cooper et al. (2016) suggested that olivine acts like a solid-solution alloy, for which mobile dislocation glide velocities are often limited by interactions with solute atoms rather than by dislocation climb. There are a variety of potential mechanisms by which solute atoms can interact with dislocations (for a review, see Chapter 5 in Kassner, 2015), and the macroscopic behavior associated with these mechanisms is consistent with the behavior of many minerals. Furthermore, in the context of the development of a CPO, it does appear that solute effects on dislocation velocities can be anisotropic (e.g., Akhtar and Teghtsoonian, 1969).

3.1.2 Grain rotations not controlled by dislocation motion

Grains in an aggregate may rotate by means other than the motion of lattice defects. The interfaces between neighboring grains, the grain boundaries, can be orders of magnitude weaker than the grain interiors (e.g., Jackson and Faul, 2010), allowing grains to translate past one another. This grain-boundary sliding has long been thought to modify grain rotations in deforming rocks (e.g., Boullier and Gueguen, 1975), although the manner in which rotations are affected is still not agreed upon. Confusion arises from the manner in which sliding on boundaries is accommodated at triple junctions and other grain-boundary irregularities. If that accommodation is by the nucleation and motion of lattice dislocations, the rotations association with dislocation motion can outweigh those associated with grain-boundary sliding (Hansen et al., 2014, 2012b, 2011). If that accommodation is by diffusion of material away from stress concentrations (i.e., diffusion creep), the controls on grain rotations are less clear (e.g., Sundberg and Cooper, 2008).

Diffusion creep is generally considered to randomize grain orientations and destroy seismic anisotropy (e.g., Behn et al., 2009; Karato and Wu, 1993). However, several studies have demonstrated through simulation (Wheeler, 09/2009) and experiments (Maruyama and Hiraga, 2017a; Miyazaki et al., 2013) that CPO can be preserved and even created if diffusion creep is the dominant deformation mechanism. In the most intuitive models for CPO generated from this mechanism, rotations controlled by the grain shape and grain shape controlled by crystallography are both required.

3.1.2.1 Influence of grain shape on grain rotations

As grain-boundaries are relatively weak, the role of grain shape in controlling grain rotations can be evaluated by considering a rigid particle embedded in a viscous medium. The original equations of motion were derived by Jeffery (Jeffery, 1922) and first applied to rocks in the mid 1960s (Bhattacharyya, 1966; Gay, 1968, 1966). In this approach, elongate grains rotate freely and their rate of rotation is controlled by both their aspect ratio and the fluid velocity gradients (Fernandez, 1987;

Ildefonse et al., 1992), a system that is perhaps best applied to dispersed crystals suspended in a melt.

The physics of grain rotation are complex due to the interactions among neighboring grains. Ildefonse et al. (1992) demonstrated with analog experiments that concentrated suspensions of elongate grains will asymptotically approach steady orientation distributions due to the so-called “tiling effect”. In simple shear, the long axes of grains tend to align with the shear direction. In coaxial flow, the long axes tend to align in the planes of maximum extension. The comparison between grain rotations in a concentrated suspension and those in a dense aggregate of grains is not straightforward due to the enhanced mechanical interaction among neighboring grains of the latter. However, recent experiments on olivine aggregates in the diffusion creep regime by Miyazaki et al. (2013) have demonstrated asymptotic alignment among elongated grains in a manner qualitatively consistent with the expected result from concentrated suspensions of particles. This relationship implies that in diffusion creep, a considerable amount of the total strain is taken up by sliding on grain boundaries.

Rotations associated with elongated grain shapes will lead to crystallographic alignment if the grain shapes are crystallographically controlled. In two-phase aggregates, anisotropy in the interfacial energy leads to crystallographically controlled habit. This effect has been observed in aggregates of forsterite + diopside and forsterite + anorthite (Miyazaki et al., 2013), leading to grains typically elongated along [100]. As illustrated in Figure 4, during deformation, these elongated olivine grains tend to align with their [100] axes normal to the compression direction or parallel to the tension direction, respectively. Similar effects have been observed in aggregates of olivine + melt. Olivine crystals in mafic melts have been observed in natural and laboratory settings to consistently have grain shapes that are shortest in the [010] direction, with crystal dimensions of similar length in the [100] and [001] directions (Donaldson, 1976; Drever and Johnston, 1958; Fleet, 1975; Schwindinger and Anderson, 1989). Qi et. al (2018) recently observed a similar link between olivine grain shapes and crystallography in sheared aggregates of olivine + basalt. They suggested that the shape preferred orientation led to strong alignment of [010] with the shear plane and [100] and [001] axes dispersed in

the shear plane, although this pattern was complicated by additional contributions from dislocation-based processes.

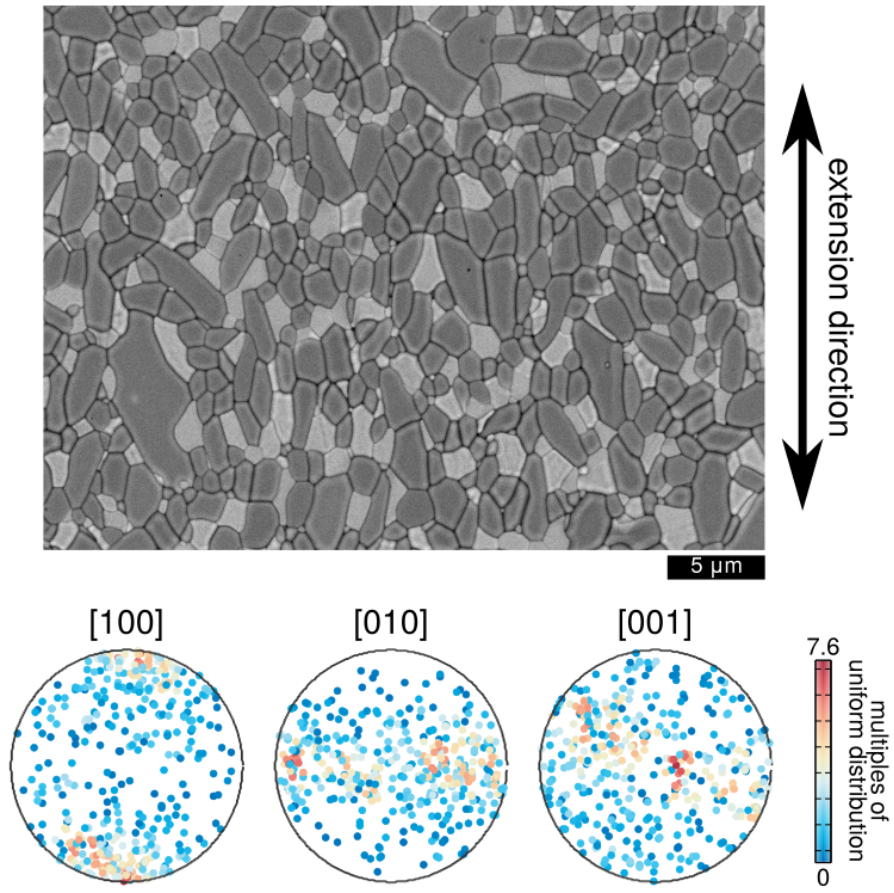

Figure 4: Example of CPO induced by formation of a shape-preferred orientation in a mixture of forsterite and diopside (sample KS-14) originally presented by Miyazaki et al. (2013). A backscattered electron image illustrates the elongate grains of forsterite (dark gray) and diopside (light gray) that have aligned during vertical extension of the sample. The orientation distribution presents orientations of forsterite grains, indicating alignment of [100] with the extension direction.

In addition to the first-order role of grain shape in influencing grain rotations, crystallographically controlled grain shapes will also be linked to higher frequencies of certain types of grain boundaries. Miyazaki et al. (2013) and Maruyama and Hiraga (2017a, 2017b) observed elongate grains in forsterite + diopside aggregates and noted an abundance of long and straight interfaces parallel to (010). They hypothesized that grain-boundary sliding occurs more easily on these boundaries (i.e.,

there is a lower grain-boundary viscosity), which will in turn additionally modify grain rotations and the eventual CPO. Although direct evidence remains to be obtained for variability in the viscosity of olivine grain boundaries, there is indirect evidence of variability in other physical properties of olivine grain boundaries, such as electrical conductivity (Pommier et al., 2018).

Importantly, this link between grain shape, grain-boundary sliding, and CPO can apparently lead to formation of seismic anisotropy in deformation regimes that exhibit very little dislocation activity. The experiments of Miyazaki et al. (2013) record rheological behavior largely consistent with diffusion creep as the primary deformation mechanism. This observation contradicts the conventional wisdom that anisotropic regions of Earth's mantle are deforming by dislocation creep and isotropic regions are deforming by diffusion creep (e.g., Karato and Wu, 1993). Numerical experiments by Wheeler (09/2009) support this new perspective and demonstrate that elongate grain shapes help to stabilize CPOs during deformation by diffusion creep and can even lead to macroscopic anisotropy in viscosity (Wheeler, 2010).

3.2 Extrinsic anisotropy

Extrinsic anisotropy can result from the spatial arrangement of multiple phases in a rock with different elastic properties. Thus, in the case of elastic waves with a wavelength much greater than the inherent length scale of the spatial distribution of phases, anisotropy in the phase distribution can lead to macroscopic seismic anisotropy, even if the individual phases are not intrinsically anisotropic. Furthermore, extrinsic anisotropy can also result from specific spatial arrangements of different rock types, such as layering of lithologies with very different elastic properties, whether or not the individual rocks types are not intrinsically anisotropic.

3.2.1 Calculating extrinsic anisotropy

The simplest approach to extrinsic anisotropy is to consider a layered medium in which each layer is isotropic. An early treatment of this problem was given by Backus (1962). If we consider deformation parallel to the layers, then each layer will support a different stress, but each layer will undergo the

same strain. If we consider deformation perpendicular to the layers, then each layer will undergo different strains, but each layer will undergo the same stress. If the characteristic length scale of the layering is sufficiently small compared to the wavelength of the elastic waves propagating through the medium, this layering results in a transversely isotropic medium (i.e., hexagonal symmetry) with the symmetry axis normal to the layering. A medium of this type is often referred to as a smooth, transversely isotropic, long-wavelength equivalent (Fitchner et al. 2013). Azimuthal anisotropy would not be detected by horizontally propagating waves if the layering is horizontal. There is, however, radial anisotropy defined by

$$\xi = \langle \mu \rangle \left\langle \mu^{-1} \right\rangle , \tag{1}$$

where μ is the shear modulus of an isotropic layer, and the angled brackets indicate the volume average over all layers.

Further developments have been presented for cases in which the individual layers are anisotropic. If the individual layers are themselves transversely anisotropic with symmetry axes normal to the layering, then the elastic properties of the effective medium can be calculated using the Love parameters of those layers (e.g., equations 1 and 2 in Fichtner et al. 2013). Nayfeh (1995, equation 15.49) presents a solution for calculating the full stiffness tensor of the effective medium if the individual layers have orthotropic anisotropy (i.e., orthorhombic symmetry) with two symmetry axes parallel to the layering and the third normal to the layering. Methods also exist for calculating the full stiffness tensor for the effective medium if the individual layers have arbitrary anisotropy in any orientation (e.g., equation 5 in Schonberg and Muir, 1982).

Extrinsic anisotropy resulting from features dispersed within a medium rather than discrete layers (i.e., foliated and lineated mineral fabrics or the presence of fluid-filled cracks) is generally calculated with more complex mathematical models such as the self-consistent scheme or the differential effective medium (Faccenda et al., 2019; Kendall, 2000; Mainprice, 1997). These effective-medium methods allow calculation of the elastic tensor of a representative volume element characterized by

the presence of ellipsoidal inclusions of one (or more for the self-consistent scheme) phase(s) dispersed in a matrix with contrasting elastic properties.

3.2.2 Mechanisms of producing extrinsic anisotropy

Observations from exhumed peridotite massifs indicate that a range of compositional fabrics exist in the upper mantle and that these fabrics may contribute to seismic anisotropy. Nearly all massifs exhibit compositional variability (e.g., Bodinier et al., 2014; Python and Ceuleneer, 2003; Quick, 1981), however systematic layering, characterized by alternating bands of pyroxene-rich and pyroxene-poor peridotite, is less common. Examples of layering include the Josephine (e.g., Loney and Himmelberg, 1976), Horoman (Niida, 1974), Erro-Tobbio (Rampone and Borghini, 2008), and External Liguride (Borghini et al., 2016) peridotite massifs. The segregation of a melt phase into melt-rich bands in regions of high strain rate is another possible source of extrinsic anisotropy in the upper mantle (e.g., Holtzman and Kendall, 2010). In exhumed massifs, observations of foliated plagioclase lherzolites include sections of the Trinity (Quick, 1981), Lanzo (Higgie and Tommasi, 2014), Erro-Tobbio (Piccardo and Vissers, 2007), and Othris (Dijkstra et al., 2001) massifs. The elongation of individual grains can also lead to foliated and lineated fabrics that can be a source of extrinsic anisotropy, if the contrast in isotropic elastic moduli between mineral phases is large enough (Faccenda et al., 2019). However, while the CPOs of mineral phases are often assessed in detail, the role of compositional layering for extrinsic anisotropy is rarely evaluated. As an example of the seismic anisotropy produced by compositional layering, in Figure 5 we calculate the contrast between harzburgite and dunite, based on fabrics measured in the Josephine Peridotite.

Relatively few models describe the formation of mineralogical fabrics in upper mantle rocks. Infiltration of a melt phase that is out of chemical equilibrium with the host rock can lead to segregation and channelization of flow, typically through formation of dunitic melt channels in peridotite (Kelemen et al., 1995). This process has been investigated through field observations (e.g., Kelemen et al. 2000), numerical simulations (Spiegelman et al., 2001; Weatherley and Katz, 2012),

and laboratory experiments (Daines and Kohlstedt, 1994; Pec et al., 2017, 2015). Reactive melt transport during deformation can produce multiple, overprinting, compositional fabrics, as observed in the Lherz massif (e.g., Le Roux et al., 2008). This interplay has been explored experimentally (D. S. H. King et al., 2011) and numerically (Keller et al., 2017; Weatherley and Katz, 2012), but has not been quantitatively tested against outcrop-scale observations. A useful review of geological observations related to forming compositional heterogeneity is provided by Tommasi and Vauchez (2015).

In contrast, a variety of models exist describing the segregation of melt into anisotropic structures in partially molten rocks. At the grain scale, a melt phase will locally rearrange along olivine grain boundaries in an anisotropic manner dependent on the interfacial energies (e.g., Waff and Faul, 1992) or the orientation of the maximum principle stress (e.g, Daines and Kohlstedt, 1997). Typical models consider the melt to reside in spherical, ellipsoidal (Faul et al., 1994; Tommasi et al., 2006; Vauchez et al., 2000; Waff and Faul, 1992), or tubular pores (Mavko, 1980). All of these scenarios serve to reduce seismic velocities of mantle rocks. However, if the melt pores are also aligned, they will impart anisotropy in addition to any intrinsic anisotropy produced by the crystalline matrix. An analysis and comparison of these different models is provided by Blackman and Kendall (1997). At longer length scales, melt can segregate into melt-rich bands during deformation (e.g., Holtzman et al., 2003; King et al., 2010). The dynamics of melt segregation during deformation were recently reviewed by Kohlstedt and Holtzman (2009) and its effect on seismic anisotropy quantified by Holtzman and Kendall (2010).

3.2.3 The interplay between intrinsic and extrinsic anisotropy

To explore the interplay between extrinsic and intrinsic anisotropy (Figure 5), we first consider a natural example of mantle layering from the Josephine Peridotite in Southwestern Oregon (Hansen and Warren, 2015; Warren et al., 2008). Some sections of the Josephine Peridotite are composed of alternating, centimetric layers of dunite and harzburgite (Kelemen and Dick, 1995; Loney and

Himmelberg, 1976), each of which is intrinsically anisotropic due to the crystallographic alignment of olivine and orthopyroxene. The shape and orientation of the anisotropy is largely similar between the two layers, although the magnitude is larger in the dunites (Figure 5). The relatively small differences in seismic velocity between the two rock types primarily results from the presence of orthopyroxene in the harzburgites.

We calculated the effective anisotropy of a layered composite assuming equal volumes of dunite and harzburgite and using the method of Schonberg and Muir (1982). From the prediction for the combined effect of intrinsic and extrinsic anisotropy presented in the upper right panel of Figure 5, the anisotropy is clearly dominated by the intrinsic anisotropy of the layers. This result is supported by 3-D simulations of wave propagation by Faccenda et al. (2019), which demonstrate that, for a variety of compositional fabrics, the extrinsic anisotropy is only significant if the individual components have large differences in elastic moduli. In perhaps the most extreme case, Tommasi and Vauchez (2015) investigated the anisotropy of layered peridotites and pyroxenites, in which the pyroxenites contained considerable amounts of garnet. Even then, the anisotropy is dominated by the intrinsic anisotropy, and in fact, the overall anisotropy is diminished slightly because of the low anisotropy of the garnet. Thus, it seems that compositional layering will only be the primary source of anisotropy in the absence of a CPO or aligned melt. However, the review by Tommasi and Vauchez (2015) also highlights that the formation of compositional layering in nature generally involves deformation (inducing a CPO) and/or the mobilization of a melt phase (leading to aligned melt pockets), and therefore it seems the role of solid-state heterogeneity in observed anisotropy will be negligible.

As an alternative example, we consider the anisotropy of the same system modified to include an isotropic distribution of basaltic melt within the dunite layers. The role of a melt phase in moderating seismic velocity and anisotropy depends on the grain scale geometry of the melt distribution. We opted to scale the velocities of the dunites in an isotropic manner to examine the role of an isotropic melt distribution (Blackman and Kendall, 1997). An isotropic reduction in the velocity of the dunites

517

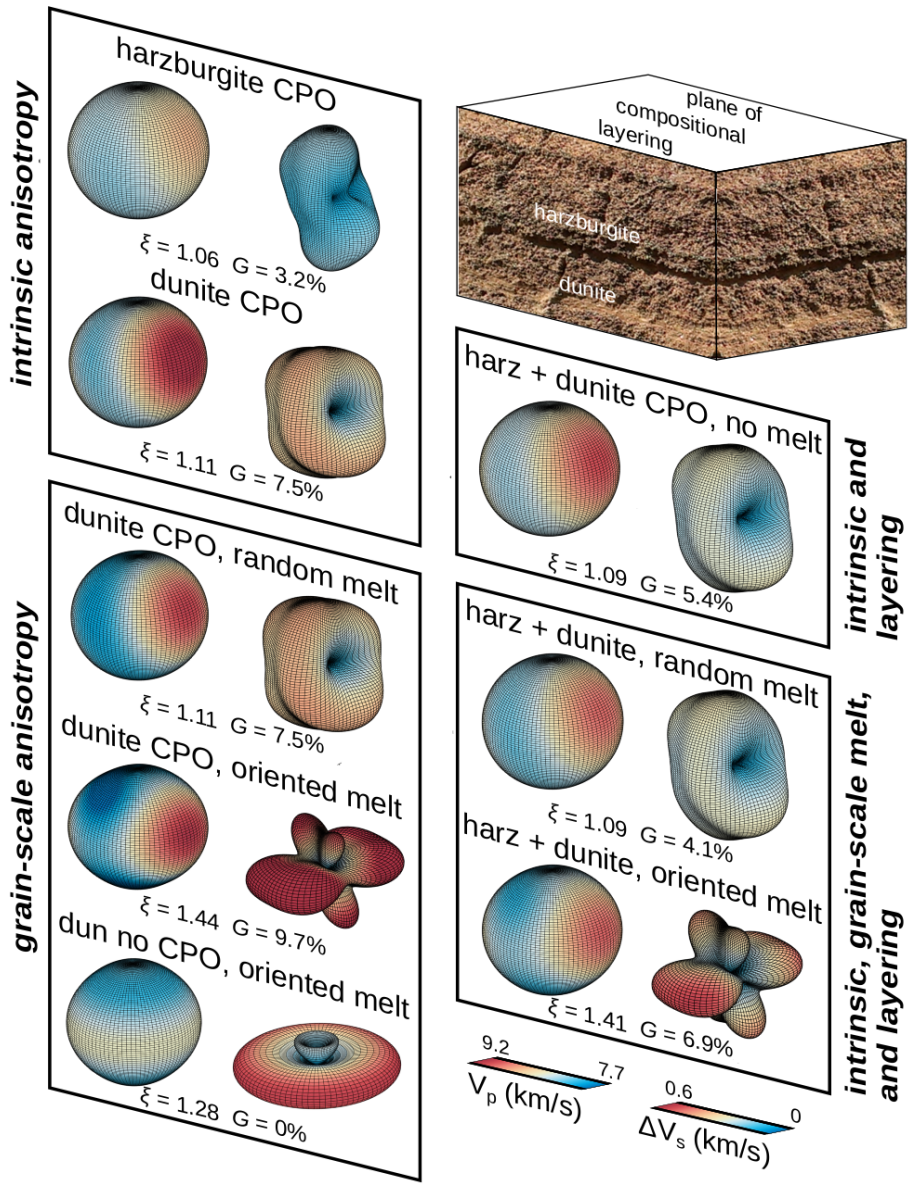

Figure 5: Demonstration of extrinsic seismic anisotropy and its interaction with typical intrinsic anisotropy in naturally deformed peridotites. Photo shows compositional layering in the Josephine Peridotite (vertical dimension is ~0.5 m). Examples of intrinsic anisotropy in a harzburgite and dunite are from Josephine Peridotite samples 3924J07 (IGSN IEJMW000D) and 3924J08 (IGSN IEJMW000E), respectively, originally described by Warren et al. (2008). CPOs from both olivine and orthopyroxene are included in calculations for the harzburgite. Three

dimensional diagrams are given for the directional dependence of P-wave velocities, and the directional dependence of the difference in S-wave velocity between the two S-wave polarizations. The local radius of each diagram is proportional to the magnitude of the velocity (or difference in velocities) for waves propagating parallel to that radius. The upper-left panel presents only the intrinsic anisotropy, and the upper-right panel presents the intrinsic anisotropy combined with the extrinsic anisotropy from layering the harzburgite and dunite. The lower-left panel presents the effect of a melt phase in the dunite for different combinations of grain-scale anisotropy and with horizontal melt pockets. The lower-right panel presents the combination of intrinsic anisotropy from a CPO and extrinsic anisotropy from a melt phase and lithological layering. Three-dimensional projections were generated with the MTEX toolbox for Matlab® (Mainprice et al., 2011).

will increase the contribution of extrinsic anisotropy to the overall anisotropy. Figure 5 implements a melt fraction of 1%, which is considerably larger than most estimates of partially molten regions in the upper mantle (e.g., Kelemen et al., 1997), even if melt is segregated into melt-rich bands (Holtzman and Kendall, 2010). However, we present this case as only at these extreme values is the difference between dunites and harzburgites large enough for extrinsic anisotropy to dominate the symmetry of the overall anisotropy.

Based on these examples, the importance of extrinsic anisotropy relative to intrinsic anisotropy depends strongly on the contrast in isotropic elastic properties of the constituent materials in the composite medium. Holtzman and Kendall (2010) numerically investigated the interplay between intrinsic olivine anisotropy and extrinsic anisotropy from the segregation of a basaltic melt into oriented melt pockets and melt-rich bands. They found that the addition of a melt phase significantly increases the magnitude of p-wave and s-wave anisotropy and modifies the symmetry and orientation of the s-wave anisotropy. However, the addition of a melt phase does not seem to significantly affect the symmetry and orientation of the p-wave anisotropy or the general orientation of the fast s-wave

polarization direction. Similar results were obtained by Vauchez et al. (2000), who investigated the combined anisotropy from olivine CPO and melt pockets in the context of continental rifts, and by Tommasi et al. (2006), who investigated the combined anisotropy from olivine CPO, pyroxene CPO, and melt pockets in a peridotite massif in the Canadian Cordillera.

In general in the upper mantle, a grain- or rock-scale shape preferred orientation does not generate substantial seismic anisotropy (Faccenda et al., 2019), while the presence of preferentially aligned fluid-filled cracks or fluid-rich bands controls the anisotropic signal even at very low porosities (Faccenda et al., 2008; Mainprice, 1997). Therefore, care must be taken if interpreting seismological signals in terms of the relative contributions of intrinsic and extrinsic anisotropy. In fact, synthetic tests by Fichtner et al. (2013) revealed that most seismological data cannot definitively distinguish between intrinsic and extrinsic anisotropy.

3.3 Influence of strain on anisotropy

Anisotropy in the mechanical properties of rocks is strongly linked to their deformation history. In the case of intrinsic anisotropy, grain rotations occur in parallel with ductile strain, and therefore the evolution of the distribution of crystallographic orientations depends strongly on the magnitude and geometry of strain. In the case of extrinsic anisotropy, the spatial distribution of phases also depends strongly on the magnitude and geometry of strain. The influence of strain on the development of seismic anisotropy was recently reviewed by Skemer and Hansen (2016), and so we only briefly cover this topic here.

The primary metric used to evaluate the evolution of CPO in olivine-rich rocks has been the average orientation of [100], the seismically fast axis, relative to the shear plane and shear direction during simple shear. Experiments on dry olivine (Bystricky et al., 2000; Hansen et al., 2014; Zhang and Karato, 1995) reveal that the average [100] orientation initially follows the long axis of the finite strain ellipse and then quickly aligns with the shear direction after shear strains of 1 to 2. Experiments on moderately wet olivine (several 100 ppm H/Si) reveal that the average [100] orientation is initially

antithetic to the finite strain ellipse, but also eventually rotates into parallelism with the shear direction (Jung et al., 2006; Katayama et al., 2004).

In addition to the orientation distribution of [100], the [010] and [001] distributions also reveal systematic evolutions until a steady-state texture is reached. For dry olivine aggregates (Bystricky et al., 2000; Hansen et al., 2014; Zhang and Karato, 1995), the average [010] orientation eventually aligns with the shear-plane normal. For moderately wet olivine aggregates (Jung et al., 2006; Katayama et al., 2004), the average [001] orientation eventually aligns with the shear plane normal. These combinations of [100] parallel to the shear direction and either [010] or [001] normal to the shear plane helped support the interpretation that weak slip systems control the final texture, with [100](010) or [100](001) being dominant in either case, respectively. However, Hansen et al. (2014) noted that, during torsion of dry olivine aggregates, the [010] and [001] axis distributions undergo a protracted evolution in which they initially form girdles normal to the shear direction before finally forming distinct clusters. The evolution appears to require shear strains of ~10 before steady-state CPOs are reached. Hansen et al. (2014) interpreted the slow evolution of the girdled fabrics to result from the comparable activity of the (010)[100] and (001)[100] slip systems (e.g., Bai et al., 1991). Importantly, the girdled CPOs at moderate strain result in seismic anisotropy that has hexagonal symmetry, with a symmetry axis parallel to the shear direction. Because this hexagonal anisotropy evolves to orthorhombic symmetry at high strain, seismologically detecting transitions in the symmetry of anisotropy may provide a means to, at least qualitatively and in conjunction with the magnitude of anisotropy, map low- strain domains in the upper mantle.

These experimental results are in broad agreement with observations in naturally deformed peridotites. In a few outcrop-scale shear zones in ultramafic massifs, strain markers are present that allow the CPO to be correlated with the magnitude of strain (Hansen and Warren, 2015; Kumamoto et al., n.d.; Warren et al., 2008; Webber et al., 2010). The general observation is that the average [100] orientation reorients much slower (about a factor of 2 in shear strain) in naturally deformed aggregates

than in experimentally deformed aggregates (see Figure 3 in Skemer and Hansen, 2016). Hansen and Warren (2015) additionally looked at the degree of girdling in [010] and [001] distributions and noted that naturally deformed dunites exhibit girdling that evolves on a similar strainscale to those deformed in the laboratory.

In addition to the dependence of anisotropy on the magnitude of strain, significant differences arise in anisotropy as a function of the geometry of strain. Tommasi et al. (1999) generated a wide variety of texture types by numerically simulating olivine CPOs formed in a range of coaxial and non-coaxial flows. Relatively few experimental studies have examined CPO evolution in geometries other than simple shear. Hansen et al. (2011) deformed aggregates in axial compression and observed a transversely isotropic anisotropy with [010] axes parallel to the loading direction and which define the symmetry axis, a result that was expected based on the simulations of Tommasi et al. (1999). Hansen et al. (2016c) also investigated experimentally a complementary deformation geometry, axial extension, which was not investigated numerically by Tommasi et al. (1999). They found distinct small-circle girdles of [100] around the extension direction, which they hypothesized resulted from the near identical strengths of the (010)[100] and (001)[100] slip systems at the conditions of the experiments.

The effect of strain geometry on CPO in naturally deformed rocks has been evaluated in a few studies. Chatzaras et al. (2016) and Bernard et al. (2019) both used the shape-preferred orientation of spinel grains as a proxy for strain geometry in naturally deformed peridotite xenoliths. These studies concluded that the olivine CPO correlates with the strain geometry. Kumamoto et al. (2019)found that CPO evolution in outcrop-scale transects of shear zones in the Josephine Peridotite are best explained by a combination of simple shear and extension.

So far, we have considered the evolution of anisotropy from a uniform[3] initial texture. However, the

[3] Many authors erroneously refer to very weak textures as “random”. In the context of orientation distributions, random simply means that orientations are drawn at random from a particular distribution, but that distribution could actually describe a very strong CPO. In contrast, “uniform” refers to a uniform distribution, for which all orientations are equally probable (i.e., there is no distinct preferred orientation).

deformation history of mantle rocks can be long and complicated, and therefore, the deformation process of interest is often superimposed on an already textured rock. Several authors have examined the role of initial CPOs on the subsequent evolution of anisotropy. Boneh and Skemer (2014), in particular, conducted triaxial compression experiments on samples of natural olivine with a strong initial texture and systematically varied the orientation of the initial texture relative to the loading axes. Each initial texture orientation resulted in a different evolution of CPO and thus seismic anisotropy. Hansen et al. (2016c) conducted experiments on dry olivine aggregates in which deformation was initially imposed in extension and subsequently imposed in torsion. Hansen et al. (2016a) identified differences in the CPO evolution through comparison of these experiments to experiments conducted solely in torsion. The evolutionary paths of anisotropy in experiments on initially uniform samples and samples with strong initial CPOs tend to converge at high strains (>5 shear strain for the case of simple shear). Thus, considering the full history of CPO evolution is primarily important in regions of the upper mantle that have undergone relatively little recent strain in the current strain geometry.

Unfortunately, very little information is available for the evolution of extrinsic anisotropy with increasing strain, which will likely depend on the mechanisms leading to compositional layering. Holtzman and Kendall (2010) demonstrated that the degree of melt segregation in the olivine + melt system is quantitatively linked to seismic anisotropy. The link between the degree of melt segregation and the total strain is complex but has been parameterized in an empirical model by King et al. (Holtzman et al., 12/2012). Further investigation of the evolution of extrinsic anisotropy is a clear target for future research.

4 The longevity of anisotropy

A variety of geodynamic settings involve portions of the upper mantle in which anisotropy is assumed to be preserved from previous formation and deformation events. These settings include “freezing in” of upper mantle to create the oceanic lithosphere (Becker et al., 2014; e.g., Beghein et al., 2014;

Hansen et al., 2016b; Russell et al., 2019), construction of continental interiors (e.g., Conrad et al., 2007; Marone and Romanowicz, 2007; Silver and Chan, 1988; Yuan and Romanowicz, 2010), and rifting of continental margins (e.g., Tommasi and Vauchez, 2001).

These interpretations rely on a lack of modification of the anisotropy once the anisotropy-forming process has ceased. However, Boneh et al. (2017) demonstrated that grain growth during annealing of pre-deformed olivine aggregates will modify existing CPOs, weakening and rotating the intrinsic anisotropy. Similar observations have been made for other mineral systems, including quartz (e.g., Heilbronner and Tullis, 2002), calcite (Ghosh et al., 2017), and ice (e.g., Montagnat et al., 2015). Unfortunately, the timescales of this modification are not yet well quantified. Relaxation of extrinsic anisotropy associated with mineralogical layering likely requires subsequent deformation to induce phase mixing, the mechanisms and timescales of which are still the subject of active debate (Bercovici and Skemer, 2017; Cross and Skemer, 2017; Tasaka et al., 2017). Relaxation of extrinsic anisotropy associated with the segregation of a melt phase into melt-rich bands has been better quantified, with heterogeneity on the scale of 1 m relaxing over ~1 Ma and heterogeneity on the scale of 10 m relaxing over ~300 Ma (Daniel S. H. King et al., 2011). Subsequent loading in an orientation different to the original loading direction, however, may reorganize the melt significantly faster than static annealing (Pendleton et al., 2012).

4.1 Summary of systematics in anisotropy

The above discussion illustrates that seismic anisotropy of the upper mantle is influenced by a wide-range of intrinsic and extrinsic variables. In Figure 6, we attempt to summarize systematic variations in anisotropy as a function of these variables. We consider two specific aspects of anisotropy, radial and azimuthal, in a typical geographic reference frame (i.e., with the third direction parallel to Earth's radius). For shearing parallel to Earth's surface in dry, melt-free olivine (red squares), horizontal alignment of [100] is expected. Experimental samples reveal that azimuthal and radial anisotropy increase with increasing strain until values of approximately 5% and 1.1 are reached,

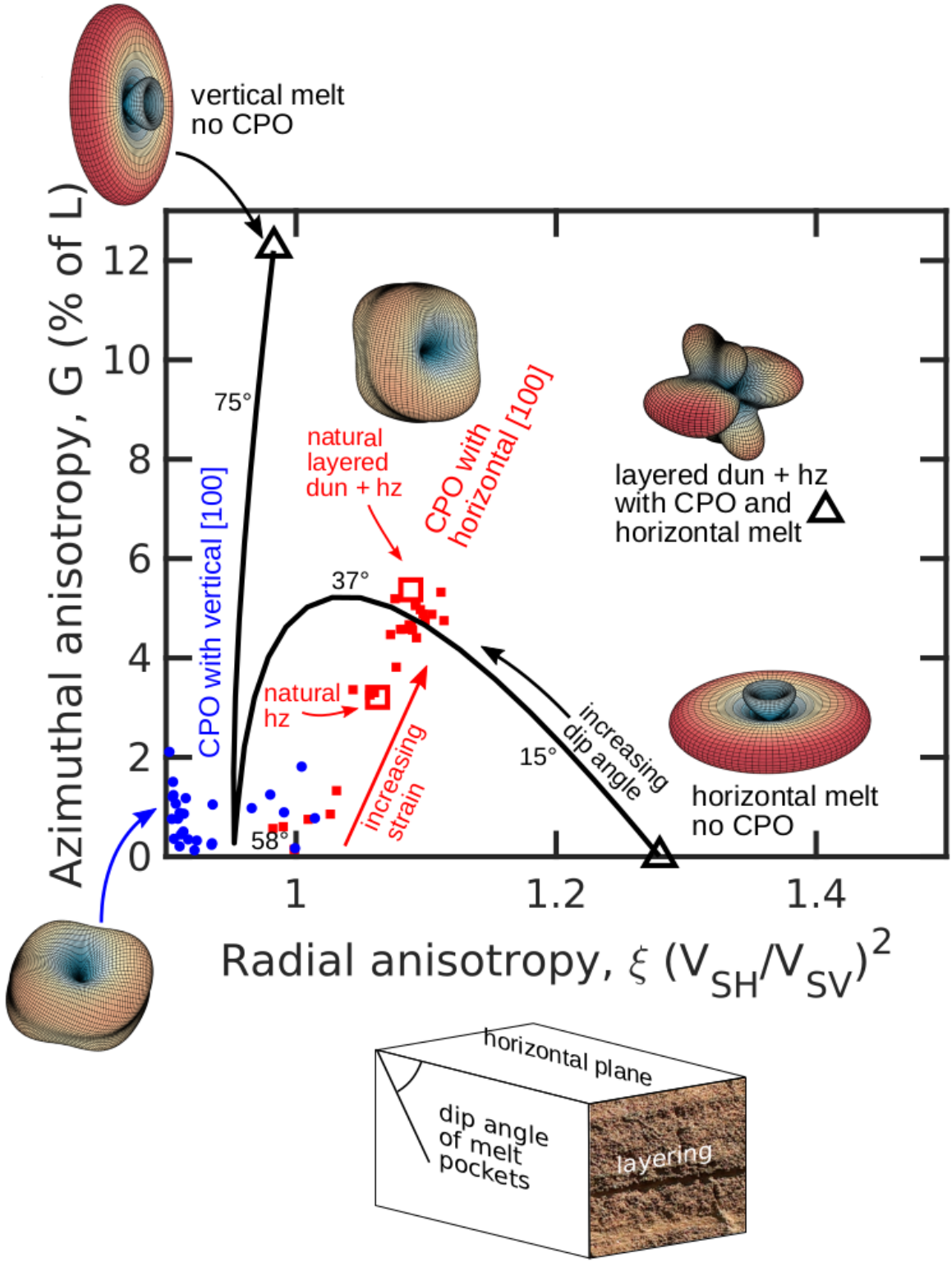

659

660 Figure 6: Systematics of azimuthal and radial anisotropy for olivine aggregates with CPO,

661 compositional layering, and/or oriented melt pockets. Only a simple set of situations are presented:

662 red data represent anisotropy with horizontal [100] maxima, blue data represent anisotropy with

vertical [100] maxima, and black data represent anisotropy of rocks including a melt phase. Solid data points are from the compilation of experimentally deformed samples in Hansen et al. (2014) assuming a mixture of 60% olivine and 40% pyroxene. Open data points are based on data from naturally deformed peridotites presented in Figure 5. Projections in 3-D represent examples of the directional dependence of ΔV_s for each scenario, as depicted in Figure 5. The block diagram presents the reference frame for layering and dipping melt pockets.

663 respectively. Natural samples (open red squares) fall on the same trend, even for the example of
664 horizontal layering of different mineral assemblages. For shear parallel to Earth's radius in dry,
665 melt-free olivine, [100] should be vertically aligned. In contrast to horizontal alignment of [100],
666 vertical alignment results in low magnitudes of azimuthal anisotropy, even if large strains have been
667 accumulated. In addition, the magnitudes of radial anisotropy are less than unity.

668 The inclusion of melt pockets leads to additional complexity. The black curve indicates the range of
669 anisotropies attainable depending on the orientation of the melt pockets and no mineral CPO.
670 Horizontal melt pockets result in high radial anisotropy and no azimuthal anisotropy. Vertical melt
671 pockets result in high azimuthal anisotropy and values of radial anisotropy just less than unity. The
672 small amount of radial anisotropy results from the fact that polarized S-waves will interact with the
673 melt pockets differently depending on propagation direction, regardless of the polarization direction.
674 That is, S-waves propagating normal to the pockets induce shear parallel to the pockets, for all
675 polarization directions, and S-waves propagating parallel to the pockets induce shear normal to the
676 pockets, for all polarization directions. Interestingly, melt-pocket orientations near 58° also result in
677 very low azimuthal anisotropy because shearing is consistently oblique to the pockets, regardless of
678 the propagation direction.

679 Clearly, the melt-pocket orientation, CPO, and mineral layering can all simultaneously contribute to
680 the anisotropy, resulting in a large parameter space to explore. For simplicity, we investigate a single
681 case involving all three contributions, in which melt pockets are horizontal, mineral layering is

horizontal, and [100] axes are horizontal. This case produces high values of both azimuthal radial anisotropy and does not fall on any of the trends previously explored.

The models in Figure 6 suggest that a combination of azimuthal and radial anisotropy constraints can be used to rule out certain mechanisms as contributing to upper mantle seismic anisotropy . Values of radial anisotropy less than unity likely cannot be explained by horizontal shearing. Radial anisotropy <1 combined with high azimuthal anisotropy likely cannot be explained by CPO or layering in melt-free rocks. Exceedingly high values of radial anisotropy (>1.1) also cannot easily be explained by CPO or layering in melt-free rocks. Very high values of both azimuthal and radial anisotropy, if observed, would likely require a combination of CPO, mineral layering, and melt.

5 Forward modeling the development of anisotropy

5.1 General approach to forward modeling

As described above, the development of anisotropy not only depends on the mechanistic details of the particular process producing anisotropy, but also on the history and geometry of deformation. Therefore, the most popular methods of forward modelling anisotropy rely on models that track and allow interaction between the microphysical mechanisms associated with anisotropy and the larger scale kinematics. A variety of models have been developed for predicting intrinsic anisotropy, and we briefly review these here. Unfortunately, very little development has occurred in the context of simulating the development of extrinsic anisotropy and this remains a key topic for future research efforts.

Equations 3 and 4 above illustrate that the glide of lattice dislocations generates strain and rotation of individual grains. To predict the elastic properties of an aggregate of grains, the rotations of a population of grains must be tracked. Although tracking the rotation of a single crystal with known boundary conditions is relatively straightforward, the interactions among neighboring, anisotropic crystals in an aggregate lead to significant difficulties in tracking rotations within a population of

grains. For a recent review of models simulating the deformation of aggregates, see Pokharel et al. (2014).

Some of the most rigorous simulations include an explicitly defined microstructure (i.e., an array of grains and grain boundaries) and track the full stress and displacement fields (e.g., Lebensohn, 2001). Full-field simulations constrain the calculation to ensure that stress equilibrium and strain compatibility are maintained throughout the model volume. That is, cavities cannot open and neighboring grains cannot become interpenetrating. Although rigorous and essential for examining heterogeneities in the stress and strain fields below the grain scale, these methods are computationally expensive and are not generally used to evaluate deformations larger than a few percent strain.

To reduce the computational complexity, mean-field models ignore heterogeneity within grains and employ one of a variety of homogenization schemes to address interactions between grains in an average sense. The simplest homogenization schemes assume that either the stress or the strain rate is the same in every grain, referred to as the Sachs model (Sachs, 1928) or the Taylor (or Taylor-Bishop-Hill) model (Bishop and Hill, 1951; Taylor, 1938). In the former, stress is homogeneous, but grains have no strain compatibility requirement (i.e., cavities can open or grains can intersect one another). In the latter, strain is homogeneous, but stress equilibrium is not maintained (i.e., the stress can be different between two neighboring material points). Because these end-member models allow the deformation (and therefore rotation) to be directly calculated for each grain, they are computationally efficient, if not perfect representations of the microphysics. Some more sophisticated approaches are discussed in the next section.

For geological materials, the Taylor model can be difficult to adapt since many minerals have too few slip systems to accommodate an arbitrary strain tensor. According to the von Mises criterion (Mises, 1928), five linearly independent slip systems are required to produce any arbitrary deformation since symmetry and volume conservation reduce the strain tensor to five independent components. Olivine, for example, has only four dominant slip systems at high temperature (see the compilation in

Tommasi et al., 2000). These slip systems can be further reduced to three, as [100](001) and [001](100) produce the same Schmid tensor and are therefore linearly dependent. However, Tielke et al. (2016) observed mechanical differences between these slip systems in experiments on olivine single crystals, suggesting that they may be independent.

5.2 Models of geologic materials

One of the major models for simulating CPO evolution in olivine and pyroxene was developed by Kaminski and Ribe (2001) and Kaminski et al. (2004) and is commonly referred to as D-Rex. This model is largely based on the Taylor model and finds the closest possible strain rate tensor for each grain given its orientation and available slip systems. Any mismatch between the best-fitting strain rate and the imposed, macroscopic strain rate necessarily means that strain incompatibilities arise in the microstructure. However, Kaminski and Ribe (2001) suggested that this approach is applicable to real aggregates if any incompatibilities are assumed to be relieved by the activation of non-dislocation-based mechanisms (e.g., grain-boundary sliding), which are assumed to not affect the grain rotations. Kaminski and Ribe (2001) also included a mechanism for dynamic recrystallization to affect the CPO evolution. Grains subject to higher stresses are presumed to have higher dislocation densities and therefore higher strain energies, resulting in these grains being gradually consumed by grains with low strain energy according to a tuneable rate parameter.

Viscoplastic-self-consistent modelling (VPSC) offers an alternate approach to modeling CPO evolution by taking a mean-field approach that attempts to account for grain interactions without imposing the Sachs or Taylor end members (Lebensohn and Tomé, 1993; Molinari et al., 1987). In these models, each grain is assumed to act as an inclusion in a homogeneous effective medium, equivalent to the elastic inclusion problem (Eshelby, 1957). The properties of the effective medium are characterized by the mechanical properties of the aggregate, but this approach inherently requires the effective medium to have a linear relationship between stress and strain rate (i.e., Newtonian). However, because plastically deforming crystals tend to have non-Newtonian rheological behavior, a

linearization scheme must be imposed. The primary difference among the various implementations of the VPSC model is the method for linearization, several of which are reviewed in application to olivine by Castelnau et al. (2008). The second-order method (Ponte Castañeda, 2002) is perhaps the most accurate linearization scheme available, as it closely approximates the mechanical response determined by full-field methods by enforcing both strain strain and stress compatibility at the grain scale, although increased accuracy comes at the cost of decreased computational efficiency.

The VPSC method requires that enough slip systems are available to fulfill the von Mises criterion, similar to the Taylor model. For VPSC models of olivine, additional fictitious slip systems are generally implemented for this purpose. The relative strengths of these fictitious slip systems are set to high values, which prevents significant contribution to grain rotations and CPO evolution. However, depending on the linearization scheme, the strength of the fictitious slip systems dramatically affects the predicted mechanical properties, with the second order method again being the best approximation of full-field models (Castelnau et al., 2008).

Although VPSC is computationally more efficient than full-field models, incorporation into larger scale simulations is still cumbersome. In a major advancement, Goulding et al. (2015) developed ANPAR, an analytical approach to VPSC. This approach parameterizes an analytical function for the spin of a grain of any orientation, which is then calibrated using the second-order linearization of VPSC. This method can reproduce the results of second-order VPSC for a wide variety of deformation geometries, with an increase in computational speed of 10^4.

A key limitation of the models described above is their poor applicability to high degrees of deformation. Full-field simulations are too computationally inefficient to model CPO evolution to strains larger than a few tens of percent. D-Rex and VPSC reasonably reproduce the average CPO orientation and symmetry observed in experiments and naturally deformed rocks up to shear strains of ~6, but they tend to overestimate the texture strength, and therefore the strength of the anisotropy, after strains of ~1 (Hansen et al., 2016a; Warren et al., 2008). Although a more complete investigation

781 of the full range of model parameters could in the future yield a better prediction of the mantle fabrics
782 and associated anisotropy using D-Rex and VPSC, two recent studies have sought to overcome these
783 limitations in strain in an alternative way.

784 In the first model, Signorelli and Tommasi (2015) developed a version of VPSC that includes effects
785 related to subgrain rotation recrystallization (CDRX-CG). By tracking individual subgrain
786 orientations and the distribution of stored strain energy among all grains and subgrains, the
787 formulation allows subgrains to become new grains according to a set of criteria based on the total
788 strain and the strain energy of the parent grain. Grain interactions are simulated according to typical
789 methods for VPSC simulation, whereas subgrain interactions are assumed to follow the Sachs model,
790 implying that subgrains are not subject to the same strain compatibility requirements as the rest of the
791 aggregate. Subgrains of slightly different orientation to their parent grain are considered new grains
792 and contribute to the CPO once a threshold misorientation is reached. These new grains introduce a
793 randomization effect that prevents texture strengths from reaching the extreme values typical of VPSC
794 simulation at high strain, and comparison between model and experimental observations appears
795 reasonable up to shear strains of at least 20.

796 The second model designed for application to high strains was proposed by Hansen et al. (2016a) and
797 is referred to here as the modified director method (MDM). This approach is more phenomenological
798 in nature than other models, as grain rotations are decoupled from the mechanical response of the
799 aggregate. Grain rotations are controlled by equation 4 and the available slip systems, but the rotation
800 rate is calculated based on the crystallographic orientation relative to the flow kinematics, scaled by a
801 tuning parameter that is unique to each slip system. Scaling rotation rate by the orientation of a vector
802 in a flow is similar to the director method used to predict viscous anisotropy in geodynamic
803 simulations (Lev and Hager, 2008a, 2008b; e.g., Moresi et al., 2003). This formulation results in the
804 need for only one model parameter per slip system to track the CPO evolution. The mechanical
805 response is dealt with separately using a modified Taylor model, and again, one tuning parameter per

slip system. The benefit of this approach is the dramatic gain in computational efficiency, especially because individual grains are tracked separately, which allows easy parallelization on a multicore computer. Because of this gain in efficiency and the relatively small number of model parameters, Hansen et al. (2016a) were able to devise an optimization routine to find the best-fit model parameters that reproduce a large dataset of experimentally derived CPOs and the associated mechanical response from experiments conducted in a variety of loading geometries and to large strains. Simulations with this model reasonably reproduce the CPO orientations and texture strengths observed in experiments and natural samples to shear strains greater than 20 as well as in a variety of more complicated loading paths.

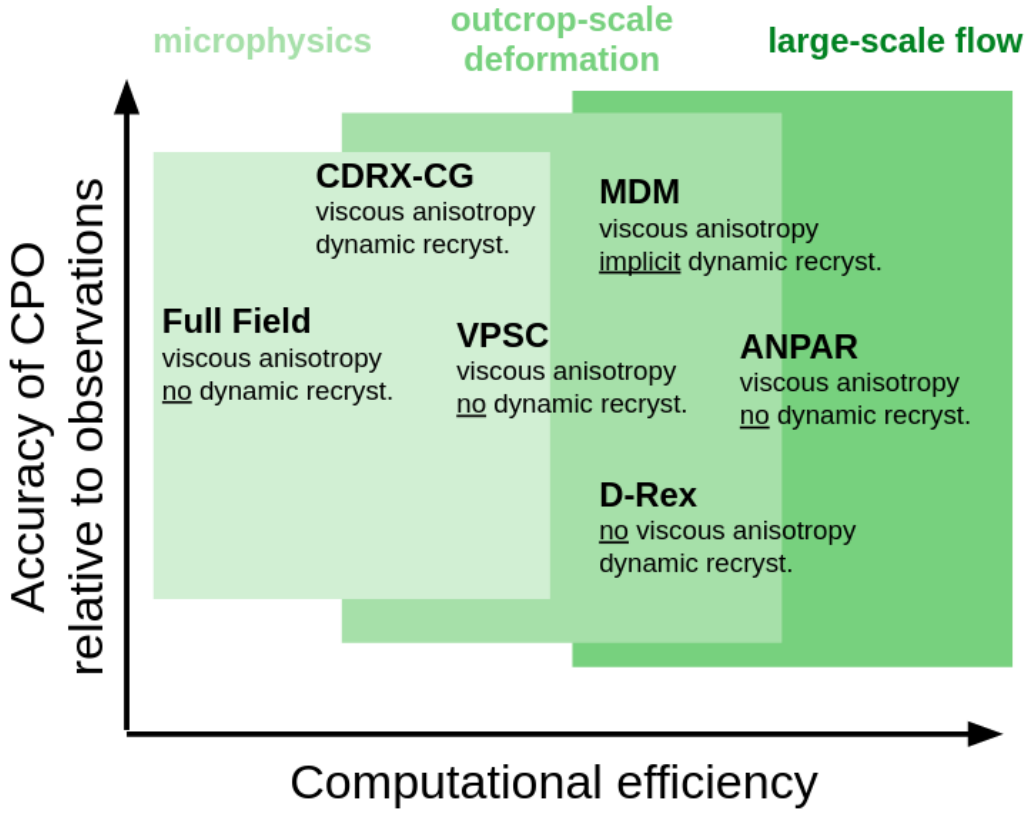

Figure 7: Schematic comparison of available models in terms of accuracy and computational efficiency. Here, accuracy refers to the ability of a model to reproduce observations in laboratory experiments and natural samples. Three fields are denoted that roughly indicate the context for which each model is best suited. All acronyms are defined in the main text.

The qualitative characteristics of the models described above are compiled in Figure 7 to help the reader distinguish which method is best suited for their purposes. In general, there is a clear tradeoff between the level of physical detail captured in the model and the computational efficiency. More detailed, physically-based models are limited to only predicting outcomes based on the physics included in the model, and are therefore probably best for testing hypotheses about microphysical processes through comparison to observations of individual textures formed under known (or estimated) conditions. More phenomenological models, which may be tuned to fit observed textures in naturally and/or experimentally deformed rocks, are better suited to large-(time or spatial) scale simulations because (1) they tend to exhibit increased computational efficiency and (2) their calibration inherently captures the effects of all the relevant microphysical phenomena. This last benefit must be treated with care, however, since calibration in this manner does not necessarily capture the proper scaling relationships for the underlying mechanisms to allow robust extrapolation across time and spatial scales.

6 Predictions of the distribution of anisotropy

Here we summarize predictions of seismic anisotropy in the upper mantle based on current knowledge of the underlying physical processes and on existing tools for forward modelling the development of anisotropy. Figure 8 presents calculations of azimuthal and radial anisotropy from intrinsic and extrinsic sources for the oceanic upper mantle. Calculations of intrinsic anisotropy were made with VPSC (Tommasi, 1998), D-Rex (Hedjazian et al., 2017), and MDM (Hansen et al., 2016b). In all cases, a flow field was calculated along with the strain-dependent development of CPO. The VPSC calculation assumes that a single deformation mechanism operates. The D-Rex calculation includes a competition between dislocation creep and diffusion creep. The MDM calibration assumes that a CPO associated with the presence of a melt is generated in the partially molten region beneath a spreading center and that a CPO associated with dislocation-based processes is generated elsewhere.

All models predict low anisotropy at the topmost and bottommost portions of upper mantle, with a

several-hundred-km thick region of higher anisotropy at intermediate depths. However, all models also predict that the region of high anisotropy is thinner for radial anisotropy than for azimuthal anisotropy. Both Hansen et al. (2016b) and Hedjazian et al. (2017) noted that the depth profile of radial anisotropy in these calculations is relatively age independent, in agreement with geophysical observations (Beghein et al., 2014; Burgos et al., 2014). Hansen et al. (2016b) suggested that this age independence results from the radial anisotropy being set primarily in the partially molten region beneath mid-ocean ridges. Hedjazian et al. (2017) suggested that it results from a transition from dislocation to diffusion creep with increasing depth. Geophysical observations suggest that depth profiles of azimuthal anisotropy do exhibit an age dependence (Beghein et al., 2014; Burgos et al., 2014; Schaeffer et al., 2016), which is predicted by the model of Hansen et al. (2016b), as well as the VPSC model of Tommasi (1998). In contrast, the transition in deformation mechanisms in the model of Hedjazian et al. (2017) results in age-independent azimuthal anisotropy.

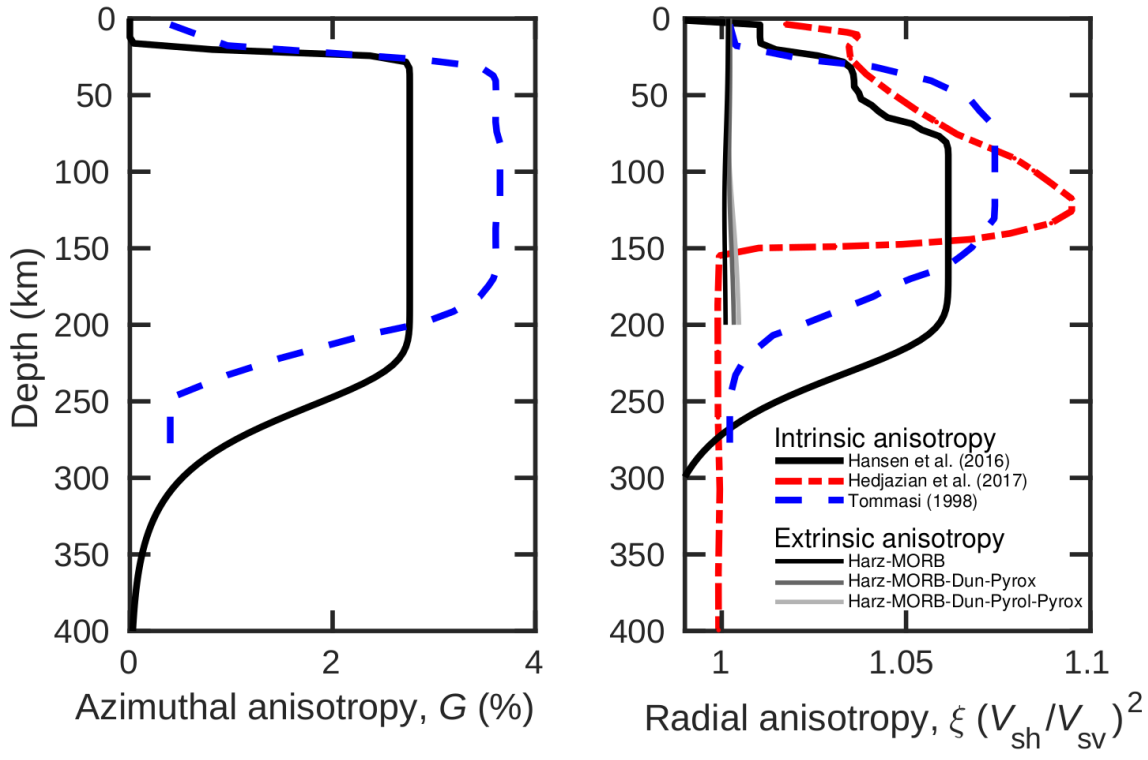

Figure 8: Synthetic profiles of anisotropy predicted for the upper mantle. Both azimuthal and radial anisotropy are presented as a function of depth. Models of intrinsic anisotropy are taken

from previously published work. Models for extrinsic anisotropy are derived in the present work and described in detail in the main text.

We also explore predictions of anisotropy from extrinsic mechanisms. In this calculation, the distribution of mafic and ultramafic lithologies in ophiolites, orogenic massifs, and seafloor samples provides the basis for our compositional model of oceanic lithosphere. The Oman Ophiolite, an ~20 km thick sequence of oceanic lithosphere, provides constraints on lithospheric structure at relatively fast spreading rates (e.g., Nicolas and Boudier, 2000). The exposed sequence consists of extrusive lavas (0.5–2 km), sheeted dikes (1–1.5 km), gabbros (0.5–6 km) and up to 12 km of the uppermost lithospheric mantle (e.g., Bodinier et al., 2014; Lippard, 1986). The mantle section consists predominantly of harzburgite, with more fertile facies (i.e., more clinopyroxene rich peridotite) near the based of the mantle section (e.g., Godard et al., 2000; Takazawa et al., 2003). Dunites occur as ~5–15% of the mantle section (Boudier and Coleman, 1981; e.g., Lippard, 1986), where they are interpreted as the channels by which melt is transported out of the mantle (Kelemen et al., 1995). Observations at slower spreading rates indicate that some melt is trapped in the upper mantle, resulting in thinner crust overlying a zone of crust-mantle mixture (e.g., Cannat, 1996; Dick et al., 2003; Sleep and Warren, 2014). Hence, our generic model for the upper oceanic lithosphere is a mixture of 45% harzburgite, 10% dunite, and 45% MORB over a 20 km depth.

Various models (Hofmann, 1988; Ringwood, 1975; Salters and Stracke, 2004; Workman and Hart, 2005) are available for the composition of the upper mantle below the plate. Here, we use pyrolite, an approximate composition for the upper mantle first developed by Ringwood (1975). Our model includes 5% pyroxenite, which is garnet bearing below 60 km, as suggested by field observations of peridotites (Bodinier et al., 2014) and the geochemistry of mid-ocean ridge basalts (Hirschmann and Stolper, 1996).

Based on this view of upper-mantle composition, we present three separate calculations for extrinsic anisotropy in the right panel of Figure 8. In the first case, as an end member, we assume that the upper

100 km of the upper mantle is interlayered harzburgite and basalt in equal proportions. In the second case, we assume the same thickness also contains layers of dunite and pyroxenite in the proportions 45:20:15:10 for harzburgite, dunite, basalt, and pyroxenite, respectively. In the third case, which we consider to be the most realistic, the uppermost 20 km is assumed to be layers of harzburgite, basalt, and dunite in the proportions 45:45:10, and the remaining 80 km is assumed to be layers of pyrolite and pyroxenite in the proportions 95:5, respectively. In all cases, we assume that compositional layering is normal to Earth's radius, and therefore the azimuthal anisotropy is zero. This orientation of layering should also produce the most extreme radial anisotropy (Figure 6). Of the three cases, the third results in the most radial anisotropy, but overall, the degree of anisotropy is substantially smaller than for predictions of intrinsic anisotropy, consistent with the predictions of Faccenda et al. (2019). Therefore, most anisotropy in the upper mantle is likely the result of intrinsic mechanisms.

7 Summary and outlook

We have presented a summary of the current state of knowledge concerning the generation of anisotropy in Earth's upper mantle based on laboratory experiments, field observations, and models. We describe the mechanisms associated with forming anisotropy, which may be derived from intrinsic or extrinsic sources, and routes to forward modelling the generation of anisotropy.

Our discussion highlights several key outstanding issues. The development of intrinsic anisotropy is well studied in experimental and natural samples, but further effort is needed to understand the microphysics that links changes in slip-system activity to physical and chemical conditions. The role of dislocation kink and jog densities in moderating dislocation velocity are of particular interest, especially in their relationship to the role of water in crystal plastic deformation. Furthermore, the role of pyroxene in decreasing the seismic anisotropy of upper mantle aggregates and changing the deformation mechanism as strain and phase mixing increases (e.g., Tasaka et al., 2017) needs to be better understood. Forward models of the development of intrinsic anisotropy are prevalent, but the most popular models do poorly at high strains and are computationally intensive. Newer generations

of models are primed to allow major improvements in forward modelling anisotropy by increasing both accuracy and efficiency at the expense of capturing the physics of the implicit processes.

The development of extrinsic anisotropy is less well studied and more observations are needed of the evolution of extrinsic anisotropy, as well as physical models that can be used to forward model this evolution. However, although less well investigated, recent evaluations of the relative contributions of different types of anisotropy suggest that extrinsic anisotropy plays a minor role throughout most of the upper mantle, unless preferentially-oriented fluid-filled cracks are present. This conclusion is supported by our comparison of forward models for predicting uppermost mantle anisotropy, which demonstrate that fitting geophysical observations of anisotropy requires a significant contribution from intrinsic anisotropy with extrinsic anisotropy playing a minor role.

Acknowledgements

The authors thank Luc Mehl for an early version of Figure 1. The authors are also grateful for the efforts of Rick Aster, Saskia Goes, and Derek Schutt in their leadership and organization of this project. Parts of this work were supported by NSF grant EAR-1625032 to JMW. The manuscript was much improved by the constructive comments of Andrea Tommasi and an anonymous reviewer.

References

Akhtar, A., Teghtsoonian, E., 1969. Solid solution strengthening of magnesium single crystals—ii the effect of solute on the ease of prismatic slip. Acta Metall. 17, 1351–1356.

Almqvist, B.S.G., Mainprice, D., 2017. Seismic properties and anisotropy of the continental crust: Predictions based on mineral texture and rock microstructure. Rev. Geophys. 55, 367–433.

Backus, G.E., 1962. Long-wave elastic anisotropy produced by horizontal layering. J. Geophys. Res.

Bai, Q., Mackwell, S.J., Kohlstedt, D.L., 1991. High-temperature creep of olivine single crystals 1. Mechanical results for buffered samples. J. Geophys. Res. [Solid Earth] 96, 2441–2463.

Becker, T.W., Chevrot, S., Schulte-Pelkum, V., Blackman, D.K., 2006. Statistical properties of seismic anisotropy predicted by upper mantle geodynamic models. J. Geophys. Res. 111, 12253.

Becker, T.W., Conrad, C.P., Schaeffer, A.J., Lebedev, S., 2014. Origin of azimuthal seismic anisotropy in oceanic plates and mantle. Earth Planet. Sci. Lett. 401, 236–250.

Beghein, C., Yuan, K., Schmerr, N., Xing, Z., 2014. Changes in Seismic Anisotropy Shed Light on the Nature of the Gutenberg Discontinuity. Science 343, 1237–1240.

Behn, M.D., Hirth, G., Elsenbeck, J.R., II, 2009. Implications of grain size evolution on the seismic structure of the oceanic upper mantle. Earth Planet. Sci. Lett. 282, 178–189.

Bercovici, D., Skemer, P., 2017. Grain damage, phase mixing and plate-boundary formation. J.

Geodyn. 108, 40–55.
Bernard, R.E., Behr, W.M., Becker, T.W., Young, D.J., 2019. Relationships between olivine CPO and deformation parameters in naturally deformed rocks and implications for mantle seismic anisotropy. Geochem. Geophys. Geosyst. https://doi.org/10.1029/2019GC008289
Bhattacharyya, D.S., 1966. Orientation of mineral lineation along the flow direction in rocks. Tectonophysics 3, 29–33.
Bishop, J.F.W., Hill, R., 1951. XLVI. A theory of the plastic distortion of a polycrystalline aggregate under combined stresses. Philos. Mag. 42, 414–427.
Blackman, D.K., Kendall, M.J., 1997. Sensitivity of teleseismic body waves to mineral texture and melt in the mantle beneath a mid–ocean ridge. Philosophical Transactions of the Royal Society of London A: Mathematical, Physical and Engineering Sciences 355, 217–231.
Bodinier, J.-L., -L. Bodinier, J., Godard, M., 2014. Orogenic, Ophiolitic, and Abyssal Peridotites. Treatise on Geochemistry. https://doi.org/10.1016/b978-0-08-095975-7.00204-7
Boioli, F., Carrez, P., Cordier, P., Devincre, B., Marquille, M., 2015. Modeling the creep properties of olivine by 2.5-dimensional dislocation dynamics simulations. Phys. Rev. B Condens. Matter 92, 014115.
Boneh, Y., Skemer, P., 2014. The effect of deformation history on the evolution of olivine CPO. Earth Planet. Sci. Lett. 406, 213–222.
Boneh, Y., Wallis, D., Hansen, L.N., Krawczynski, M.J., 2017. Oriented grain growth and modification of “frozen anisotropy”in the lithospheric mantle. Earth Planet. Sci. Lett.
Borghini, G., Rampone, E., Zanetti, A., Class, C., Cipriani, A., Hofmann, A.W., Goldstein, S.L., 2016. Pyroxenite layers in the Northern Apennines’ upper mantle (Italy)—generation by pyroxenite melting and melt infiltration. J. Petrol. 57, 625–653.
Boudier, F., Coleman, R.G., 1981. Cross section through the peridotite in the Samail ophiolite, southeastern Oman Mountains. J. Geophys. Res. [Solid Earth] 86, 2573–2592.
Boullier, A.M., Gueguen, Y., 1975. SP-mylonites: origin of some mylonites by superplastic flow. Contrib. Mineral. Petrol. 50, 93–104.
Brenner, R., Lebensohn, R.A., Castelnau, O., 2009. Elastic anisotropy and yield surface estimates of polycrystals. Int. J. Solids Struct. 46, 3018–3026.
Browaeys, J.T., Chevrot, S., 2004. Decomposition of the elastic tensor and geophysical applications. Geophys. J. Int. 159, 667–678.
Burgos, G., Montagner, J.-P., Beucler, E., Capdeville, Y., Mocquet, A., Drilleau, M., 2014. Oceanic lithosphere-asthenosphere boundary from surface wave dispersion data. J. Geophys. Res. [Solid Earth] 119, 1079–1093.
Bystricky, M., Kunze, K., Burlini, L., Burg, J.-P., 2000. High Shear Strain of Olivine Aggregates: Rheological and Seismic Consequences. Science 290, 1564–1567.
Cannat, M., 1996. How thick is the magmatic crust at slow spreading oceanic ridges? J. Geophys. Res., Geol. Soc. Spec. Publ., London 101, 2847–2857.
Carter, N.L., Ave’lallemant, H.G., 1970. High Temperature Flow of Dunite and Peridotite. GSA Bulletin 81, 2181–2202.
Castelnau, O., Blackman, D.K., Lebensohn, R.A., Ponte Castañeda, P., 2008. Micromechanical modeling of the viscoplastic behavior of olivine. J. Geophys. Res. [Solid Earth] 113.
Chang, S.-J., Ferreira, A.M.G., Ritsema, J., van Heijst, H.J., Woodhouse, J.H., 2015. Joint inversion for global isotropic and radially anisotropic mantle structure including crustal thickness perturbations. J. Geophys. Res. [Solid Earth] 120, 4278–4300.
Chatzaras, V., Kruckenberg, S.C., Cohen, S.M., Medaris, L.G., Withers, A.C., Bagley, B., 2016. Axial-type olivine crystallographic preferred orientations: The effect of strain geometry on mantle texture. J. Geophys. Res. [Solid Earth] 121, 4895–4922.
Conrad, C.P., Behn, M.D., Silver, P.G., 2007. Global mantle flow and the development of seismic anisotropy: Differences between the oceanic and continental upper mantle. J. Geophys. Res. 112, 224.

Cooper, R.F., Stone, D.S., Plookphol, T., 2016. Load relaxation of olivine single crystals. J. Geophys. Res. [Solid Earth] 121, 2016JB013425.
Cottrell, E., Kelley, K.A., 2011. The oxidation state of Fe in MORB glasses and the oxygen fugacity of the upper mantle. Earth Planet. Sci. Lett. 305, 270–282.
Crampin, S., 1981. A review of wave motion in anisotropic and cracked elastic-media. Wave Motion 3, 343–391.
Cross, A.J., Skemer, P., 2017. Ultramylonite generation via phase mixing in high-strain experiments. J. Geophys. Res. [Solid Earth] 122, 1744–1759.
Crosson, R.S., Lin, J.-W., 1971. Voigt and Reuss prediction of anisotropic elasticity of dunite. J. Geophys. Res. 76, 570–578.
Daines, M.J., Kohlstedt, D.L., 1997. Influence of deformation on melt topology in peridotites. J. Geophys. Res., Geophys. Monogr. Ser. 102, 10257–10271.
Daines, M.J., Kohlstedt, D.L., 1994. The transition from porous to channelized flow due to melt/rock reaction during melt migration. Geophys. Res. Lett. 21, 145–148.
Dick, H.J.B., Lin, J., Schouten, H., 2003. An ultraslow-spreading class of ocean ridge. Nature 426, 405–412.
Dick, H.J.B., Sinton, J.M., 1979. Compositional Layering in Alpine Peridotites: Evidence for Pressure Solution Creep in the Mantle. J. Geol. 87, 403–416.
Dijkstra, A.H., Drury, M.R., Vissers, R.L.M., 2001. Structural Petrology of Plagioclase Peridotites in the West Othris Mountains (Greece): Melt Impregnation in Mantle Lithosphere. J. Petrol. 42, 5–24.
Donaldson, C.H., 1976. An experimental investigation of olivine morphology. Contrib. Mineral. Petrol. 57, 187–213.
Drever, H.I., Johnston, R., 1958. XIII.—Crystal Growth of Forsteritic Olivine in Magmas and Melts. Transactions of the Royal Society of Edinburgh. https://doi.org/10.1017/s0080456800009509
Eakin, C.M., Rychert, C.A., Harmon, N., 2018. The Role of Oceanic Transform Faults in Seafloor Spreading: A Global Perspective From Seismic Anisotropy. J. Geophys. Res. [Solid Earth] 123, 1736–1751.
Eshelby, J.D., 1957. The determination of the elastic field of an ellipsoidal inclusion, and related problems. Proc. R. Soc. Lond. A Math. Phys. Sci. 241, 376–396.
Faccenda, M., Burlini, L., Gerya, T.V., Mainprice, D., 2008. Fault-induced seismic anisotropy by hydration in subducting oceanic plates. Nature 455, 1097.
Faccenda, M., Ferreira, A.M.G., Tisato, N., Lithgow-Bertelloni, C., Stixrude, L., Pennacchioni, G., 2019. Extrinsic Elastic Anisotropy in a Compositionally Heterogeneous Earth’s Mantle. J. Geophys. Res. [Solid Earth] 124, 1671–1687.
Faul, U.H., Toomey, D.R., Waff, H.S., 1994. Correction to “Intergranular basaltic melt is distributed in thin, elongated inclusions” by Ulrich H. Faul, Douglas R. Toomey and Harve S. Waff. Geophys. Res. Lett. 21, 505–505.
Fernandez, A., 1987. Preferred orientation developed by rigid markers in two-dimensional simple shear strain: a theoretical and experimental study. Tectonophysics 136, 151–158.
Fichtner, A., Kennett, B.L.N., Igel, H., Bunge, H.-P., 2010. Full waveform tomography for radially anisotropic structure: New insights into present and past states of the Australasian upper mantle. Earth Planet. Sci. Lett. 290, 270–280.
Fichtner, A., Kennett, B.L.N., Trampert, J., 2013. Separating intrinsic and apparent anisotropy. Phys. Earth Planet. Inter. 219, 11–20.
Fleet, M.E., 1975. The growth habits of olivine; a structural interpretation. Can. Mineral. 13, 293–297.
French, S.W., Romanowicz, B.A., 2014. Whole-mantle radially anisotropic shear velocity structure from spectral-element waveform tomography. Geophys. J. Int. 199, 1303–1327.
Frost, H.J., Ashby, M.F., 1982. Deformation mechanism maps: the plasticity and creep of metals and ceramics. Pergamon Press, Oxford, UK.

Gaboriaud, R.J., Darot, M., Gueguen, Y., Woirgard, J., 1981. Dislocations in olivine indented at low temperatures. Phys. Chem. Miner. 7, 100–104.
Gaherty, J.B., Jordan, T.H., Gee, L.S., 1996. Seismic structure of the upper mantle in a central Pacific corridor. J. Geophys. Res., Mineral Physics 101, 22291–22309.
Gay, N.C., 1968. The motion of rigid particles embedded in a viscous fluid during pure shear deformation of the fluid. Tectonophysics 5, 81–88.
Gay, N.C., 1966. Orientation of mineral lineation along the flow direction in rocks: A discussion. Tectonophysics 3, 559–562.
Ghosh, B., Misra, S., Morishita, T., 2017. Plastic deformation and post-deformation annealing in chromite: Mechanisms and implications. Am. Mineral.
Girard, J., Chen, J., Raterron, P., Holyoke, C.W., 3/2013. Hydrolytic weakening of olivine at mantle pressure: Evidence of [100](010) slip system softening from single-crystal deformation experiments. Phys. Earth Planet. Inter. 216, 12–20.
Godard, M., Jousselin, D., Bodinier, J.-L., 2000. Relationships between geochemistry and structure beneath a palaeo-spreading centre: a study of the mantle section in the Oman ophiolite. Earth and Planetary Science Letters. https://doi.org/10.1016/s0012-821x(00)00149-7
Goetze, C., Poirier, J.P., 1978. The Mechanisms of Creep in Olivine [and Discussion]. Philosophical Transactions of the Royal Society of London A: Mathematical, Physical and Engineering Sciences 288, 99–119.
Goulding, N.J., Ribe, N.M., Castelnau, O., Walker, A.M., Wookey, J., 2015. Analytical parametrization of self-consistent polycrystal mechanics: Fast calculation of upper mantle anisotropy. Geophys. J. Int. 203, 334–350.
Gouriet, K., Cordier, P., Garel, F., Thoraval, C., Demouchy, S., Tommasi, A., Carrez, P., 2019. Dislocation dynamics modelling of the power-law breakdown in olivine single crystals: Toward a unified creep law for the upper mantle. Earth Planet. Sci. Lett. 506, 282–291.
Hansen, L.N., Conrad, C.P., Boneh, Y., Skemer, P., Warren, J.M., Kohlstedt, D.L., 2016a. Viscous anisotropy of textured olivine aggregates: 2. Micromechanical model. J. Geophys. Res. [Solid Earth] 121, 2016JB013240.
Hansen, L.N., Qi, C., Warren, J.M., 2016b. Olivine anisotropy suggests Gutenberg discontinuity is not the base of the lithosphere. Proc. Natl. Acad. Sci. U. S. A. 113, 10503–10506.
Hansen, L.N., Warren, J.M., 2015. Quantifying the effect of pyroxene on deformation of peridotite in a natural shear zone. J. Geophys. Res. [Solid Earth] 120, 2717–2738.
Hansen, L.N., Warren, J.M., Zimmerman, M.E., Kohlstedt, D.L., 2016c. Viscous anisotropy of textured olivine aggregates, Part 1: Measurement of the magnitude and evolution of anisotropy. Earth Planet. Sci. Lett. 445, 92–103.
Hansen, L.N., Zhao, Y.-H., Zimmerman, M.E., Kohlstedt, D.L., 2014. Protracted fabric evolution in olivine: Implications for the relationship among strain, crystallographic fabric, and seismic anisotropy. Earth Planet. Sci. Lett. 387, 157–168.
Hansen, L.N., Zimmerman, M.E., Kohlstedt, D.L., 2012a. Laboratory measurements of the viscous anisotropy of olivine aggregates. Nature 492, 415–418.
Hansen, L.N., Zimmerman, M.E., Kohlstedt, D.L., 2012b. The influence of microstructure on deformation of olivine in the grain-boundary sliding regime. J. Geophys. Res. 117, B09201.
Hansen, L.N., Zimmerman, M.E., Kohlstedt, D.L., 2011. Grain boundary sliding in San Carlos olivine: Flow law parameters and crystallographic-preferred orientation. J. Geophys. Res. 116, B08201.
Hedjazian, N., Garel, F., Davies, D.R., Kaminski, E., 2017. Age-independent seismic anisotropy under oceanic plates explained by strain history in the asthenosphere. Earth Planet. Sci. Lett. 460, 135–142.
Heilbronner, R., Tullis, J., 2002. The effect of static annealing on microstructures and crystallographic preferred orientations of quartzites experimentally deformed in axial compression and shear. Geological Society, London, Special Publications 200, 191–218.

Hess, H.H., 1964. Seismic Anisotropy of the Uppermost Mantle under Oceans. Nature 203, 629–631.
Higgie, K., Tommasi, A., 2014. Deformation in a partially molten mantle: Constraints from plagioclase lherzolites from Lanzo, western Alps. Tectonophysics 615–616, 167–181.
Hirschmann, M.M., Stolper, E.M., 1996. A possible role for garnet pyroxenite in the origin of the “garnet signature” in MORB. Contrib. Mineral. Petrol. 124, 185–208.
Hofmann, A.W., 1988. Chemical differentiation of the Earth: the relationship between mantle, continental crust, and oceanic crust. Earth Planet. Sci. Lett. 90, 297–314.
Holtzman, B.K., Kendall, J.-M., 2010. Organized melt, seismic anisotropy, and plate boundary lubrication. Geochem. Geophys. Geosyst. 11, Q0AB06.
Holtzman, B.K., King, D.S.H., Kohlstedt, D.L., 12/2012. Effects of stress-driven melt segregation on the viscosity of rocks. Earth Planet. Sci. Lett. 359-360, 184–193.
Holtzman, B.K., Kohlstedt, D.L., Zimmerman, M.E., Heidelbach, F., Hiraga, T., Hustoft, J., 2003. Melt Segregation and Strain Partitioning: Implications for Seismic Anisotropy and Mantle Flow. Science 301, 1227–1230.
Ildefonse, B., Launeau, P., Bouchez, J.-L., Fernandez, A., 1992. Effect of mechanical interactions on the development of shape preferred orientations: a two-dimensional experimental approach. J. Struct. Geol. 14, 73–83.
Jackson, I., Faul, U.H., 2010. Grainsize-sensitive viscoelastic relaxation in olivine: Towards a robust laboratory-based model for seismological application. Phys. Earth Planet. Inter. 183, 151–163.
Jeffery, G.B., 1922. The motion of ellipsoidal particles immersed in a viscous fluid, in: Proceedings of the Royal Society of London A: Mathematical, Physical and Engineering Sciences. The Royal Society, pp. 161–179.
Jung, H., Karato S, 2001. Water-induced fabric transitions in olivine. Science 293, 1460–1463.
Jung, H., Katayama, I., Jiang, Z., Hiraga, T., Karato, S., 2006. Effect of water and stress on the lattice-preferred orientation of olivine. Tectonophysics 421, 1–22.
Jung, H., Mo, W., Green, H.W., 2009. Upper mantle seismic anisotropy resulting from pressure-induced slip transition in olivine. Nat. Geosci. 2, 73–77.
Kaminski, E., Ribe, N.M., 2001. A kinematic model for recrystallization and texture development in olivine polycrystals. Earth Planet. Sci. Lett. 189, 253–267.
Kaminski, É., Ribe, N.M., Browaeys, J.T., 2004. D-Rex, a program for calculation of seismic anisotropy due to crystal lattice preferred orientation in the convective upper mantle. Geophys. J. Int. 158, 744–752.
Karato, S.-I., Jung, H., Katayama, I., Skemer, P., 2008. Geodynamic Significance of Seismic Anisotropy of the Upper Mantle: New Insights from Laboratory Studies. Annu. Rev. Earth Planet. Sci. 36, 59–95.
Karato, S.-I., Wu, P., 1993. Rheology of the Upper Mantle: A Synthesis. Science 260, 771–778.
Kassner, M.E., 2015. Fundamentals of Creep in Metals and Alloys. Butterworth-Heinemann.
Katayama, I., Jung, H., Karato, S.-I., 2004. New type of olivine fabric from deformation experiments at modest water content and low stress. Geology 32, 1045–1048.
Keefner, J.W., Mackwell, S.J., Kohlstedt, D.L., Heidelbach, F., 2011. Dependence of dislocation creep of dunite on oxygen fugacity: Implications for viscosity variations in Earth’s mantle. J. Geophys. Res. 116, B05201.
Kelemen, P.B., Dick, H.J.B., 1995. Focused melt flow and localized deformation in the upper mantle: Juxtaposition of replacive dunite and ductile shear zones in the Josephine peridotite, SW Oregon. J. Geophys. Res. 100, 423–438.
Kelemen, P.B., Hirth, G., Shimizu, N., Spiegelman, M., Dick, H.J., 1997. A review of melt migration processes in the adiabatically upwelling mantle beneath oceanic spreading ridges. Philosophical Transactions of the Royal Society of London. Series A: Mathematical, Physical and Engineering Sciences 355, 283–318.
Kelemen, P.B., Shimizu, N., Salters, V.J.M., 1995. Extraction of mid-ocean-ridge basalt from the upwelling mantle by focused flow of melt in dunite channels. Nature 375, 747–753.

Keller, T., Katz, R.F., Hirschmann, M.M., 2017. Volatiles beneath mid-ocean ridges: Deep melting, channelised transport, focusing, and metasomatism. Earth Planet. Sci. Lett. 464, 55–68.
Kendall, J.-M., 2000. Seismic Anisotropy in the Boundary Layers of the Mantle. Earth's Deep Interior: Mineral Physics and Tomography From the Atomic to the Global Scale 133–159.
King, D.S.H., Hier-Majumder, S., Kohlstedt, D.L., 2011. An experimental study of the effects of surface tension in homogenizing perturbations in melt fraction. Earth Planet. Sci. Lett. 307, 349–360.
King, D.S.H., Holtzman, B.K., Kohlstedt, D.L., 2011. An experimental investigation of the interactions between reaction-driven and stress-driven melt segregation: 1. Application to mantle melt extraction. Geochem. Geophys. Geosyst. 12.
King, D.S.H., Zimmerman, M.E., Kohlstedt, D.L., 2010. Stress-driven Melt Segregation in Partially Molten Olivine-rich Rocks Deformed in Torsion. J. Petrol. 51, 21–42.
Kohlstedt, D.L., 2006. The Role of Water in High-Temperature Rock Deformation. Rev. Mineral. Geochem. 62, 377–396.
Kohlstedt, D.L., Hansen, L.N., 2015. 2.18 - Constitutive Equations, Rheological Behavior, and Viscosity of Rocks, in: Schubert, G. (Ed.), Treatise on Geophysics (Second Edition). Elsevier, Oxford, pp. 441–472.
Kohlstedt, D.L., Hansen, L.N., n.d. Constitutive equations, rheological behavior, and viscosity of rocks. Treatise on Geophysics.
Kohlstedt, D.L., Holtzman, B.K., 2009. Shearing Melt Out of the Earth: An Experimentalist's Perspective on the Influence of Deformation on Melt Extraction. https://doi.org/10.1146/annurev.earth.031208.100104
Kumamoto, K.M., Warren, J.M., Hansen, L.N., 2019. Evolution of the Josephine Peridotite Shear Zones: 2. Influences on Olivine CPO Evolution. J. Geophys. Res. [Solid Earth] 124, 12763–12781.
Kumamoto, K.M., Warren, J.M., Hansen, L.N., n.d. Evolution of the Josephine Peridotite shear zones, Part 2: Influences on olivine CPO evolution. J. Geophys. Res.
Lebensohn, R., 2001. N-site modeling of a 3D viscoplastic polycrystal using Fast Fourier Transform. Acta Mater. 49, 2723–2737.
Lebensohn, R.A., Tomé, C.N., 1993. A self-consistent anisotropic approach for the simulation of plastic deformation and texture development of polycrystals: application to zirconium alloys. Acta Metall. Mater. 41, 2611–2624.
Le Roux, V., Tommasi, A., Vauchez, A., 2008. Feedback between melt percolation and deformation in an exhumed lithosphere–asthenosphere boundary. Earth Planet. Sci. Lett. 274, 401–413.
Lev, E., Hager, B.H., 2008a. Prediction of anisotropy from flow models: A comparison of three methods. Geochem. Geophys. Geosyst. 9.
Lev, E., Hager, B.H., 2008b. Rayleigh–Taylor instabilities with anisotropic lithospheric viscosity. Geophys. J. Int. 173, 806–814.
Lippard, J.S., 1986. The ophiolite of northern Oman. Geological Society London Memoir 11, 178.
Loney, R.A., Himmelberg, G.R., 1976. Structure of the Vulcan Peak alpine-type peridotite, southwestern Oregon. Geol. Soc. Am. Bull. 87, 259–274.
Long, M.D., Becker, T.W., 2010. Mantle dynamics and seismic anisotropy. Earth Planet. Sci. Lett. 297, 341–354.
Long, M.D., Silver, P.G., 2008. The subduction zone flow field from seismic anisotropy: a global view. Science 319, 315–318.
Mackwell, S.J., Kohlstedt, D.L., Paterson, M.S., 1985. The role of water in the deformation of olivine single crystals. J. Geophys. Res., Geophys. Monogr 90, 11319.
Mainprice, D., 2007. Seismic anisotropy of the deep Earth from a mineral and rock physics perspective, Treatise Geophys., 2, 437--491, doi: 10.1016. B978-044452748-6.00045-6.
Mainprice, D., 1997. Modelling the anisotropic seismic properties of partially molten rocks found at mid-ocean ridges. Tectonophysics. https://doi.org/10.1016/s0040-1951(97)00122-4

Mainprice, D., Hielscher, R., Schaeben, H., 2011. Calculating anisotropic physical properties from texture data using the MTEX open-source package. Geological Society, London, Special Publications 360, 175–192.
Mainprice, D., Tommasi, A., Couvy, H., Cordier, P., Frost, D.J., 2005. Pressure sensitivity of olivine slip systems and seismic anisotropy of Earth's upper mantle. Nature 433, 731–733.
Marone, F., Romanowicz, B., 2007. The depth distribution of azimuthal anisotropy in the continental upper mantle. Nature 447, 198–201.
Maruyama, G., Hiraga, T., 2017a. Grain- to multiple-grain-scale deformation processes during diffusion creep of forsterite + diopside aggregate: 2. Grain boundary sliding-induced grain rotation and its role in crystallographic preferred orientation in rocks. J. Geophys. Res. [Solid Earth] 122, 2017JB014255.
Maruyama, G., Hiraga, T., 2017b. Grain-to multiple-grain-scale deformation processes during diffusion creep of forsterite+ diopside aggregate I: Direct observations. J. Geophys. Res.
Mavko, G.M., 1980. Velocity and attenuation in partially molten rocks. J. Geophys. Res. 85, 5173.
Mises, R. von, 1928. Mechanik der plastischen Formänderung von Kristallen. ZAMM-Journal of Applied Mathematics and Mechanics/Zeitschrift für Angewandte Mathematik und Mechanik 8, 161–185.
Miyazaki, T., Sueyoshi, K., Hiraga, T., 2013. Olivine crystals align during diffusion creep of Earth/'s upper mantle. Nature 502, 321–326.
Molinari, A., Canova, G.R., Ahzi, S., 1987. A self consistent approach of the large deformation polycrystal viscoplasticity. Acta Metall. 35, 2983–2994.
Montagnat, M., Chauve, T., Barou, F., Tommasi, A., Beausir, B., Fressengeas, C., 2015. Analysis of Dynamic Recrystallization of Ice from EBSD Orientation Mapping. Front. Earth Sci. 81.
Montagner, J.-P., Nataf, H.-C., 1986. A simple method for inverting the azimuthal anisotropy of surface waves. J. Geophys. Res. 91, 511–520.
Moresi, L., Dufour, F., Mühlhaus, H.-B., 2003. A Lagrangian integration point finite element method for large deformation modeling of viscoelastic geomaterials. J. Comput. Phys. 184, 476–497.
Moulik, P., Ekström, G., 2014. An anisotropic shear velocity model of the Earth's mantle using normal modes, body waves, surface waves and long-period waveforms. Geophys. J. Int. 199, 1713–1738.
Nataf, H.-C., Nakanishi, I., Anderson, D.L., 1984. Anisotropy and shear-velocity heterogeneities in the upper mantle. Geophys. Res. Lett. 11, 109–112.
Nayfeh, A.H., 1995. Wave Propagation in Layered Anisotropic Media: with Application to Composites. Elsevier.
Nicolas, A., Boudier, F., 2000. Large mantle upwellings and related variations in crustal thickness in the Oman ophiolite. SPECIAL PAPERS-GEOLOGICAL SOCIETY OF AMERICA 67–74.
Niida, K., 1974. Structure of the Horoman ultramafic massif of the Hidaka metamorphic belt in Hokkaido, Japan. J. Geol. Soc. Japan 80, 31–44.
Nishimura, C.E., Forsyth, D.W., 1989. The anisotropic structure of the upper mantle in the Pacific. Geophys. J. Int. 96, 203–229.
Nye, J.F., 1985. Physical Properties of Crystals: Their Representation by Tensors and Matrices. Oxford University Press.
Ohuchi, T., Kawazoe, T., Nishihara, Y., Nishiyama, N., Irifune, T., 2011. High pressure and temperature fabric transitions in olivine and variations in upper mantle seismic anisotropy. Earth Planet. Sci. Lett. 304, 55–63.
Pec, M., Holtzman, B.K., Zimmerman, M.E., Kohlstedt, D.L., 2017. Reaction infiltration instabilities in mantle rocks: an experimental investigation. J. Petrol. 58, 979–1003.
Pec, M., Holtzman, B.K., Zimmerman, M., Kohlstedt, D.L., 2015. Reaction infiltration instabilities in experiments on partially molten mantle rocks. Geology 43, 575–578.
Pendleton, M.W., Hansen, L.N., Zimmerman, M.E., Kohlstedt, D.L., 2012. Anisotropic Viscosity of Olivine-Chromite-MORB Aggregates. Presented at the Lunar and Planetary Science Conference,

adsabs.harvard.edu.
Peselnick, L., Nicolas, A., Stevenson, P.R., 1974. Velocity anisotropy in a mantle peridotite from the Ivrea Zone: Application to upper mantle anisotropy. J. Geophys. Res. 79, 1175–1182.
Piccardo, G.B., Vissers, R.L.M., 2007. The pre-oceanic evolution of the Erro-Tobbio peridotite (Voltri Massif, Ligurian Alps, Italy). J. Geodyn. 43, 417–449.
Pokharel, R., Lind, J., Kanjarla, A.K., Lebensohn, R.A., Li, S.F., Kenesei, P., Suter, R.M., Rollett, A.D., 2014. Polycrystal plasticity: comparison between grain-scale observations of deformation and simulations. Annu. Rev. Condens. Matter Phys. 5, 317–346.
Pommier, A., Kohlstedt, D.L., Hansen, L.N., 2018. Transport properties of olivine grain boundaries from electrical conductivity experiments. Contrib. Mineral. Petrol.
Ponte Castañeda, P., 2002. Second-order homogenization estimates for nonlinear composites incorporating field fluctuations: I—theory. J. Mech. Phys. Solids 50, 737–757.
Python, M., Ceuleneer, G., 2003. Nature and distribution of dykes and related melt migration structures in the mantle section of the Oman ophiolite. Geochemistry, Geophysics, Geosystems. https://doi.org/10.1029/2002gc000354
Qi, C., Hansen, L.N., Wallis, D., Holtzman, B.K., 2018. Crystallographic Preferred Orientation of Olivine in Sheared Partially Molten Rocks: The Source of the “a-c Switch.” Geochem. Explor. Environ. Analy.
Quick, J.E., 1981. Petrology and petrogenesis of the Trinity peridotite, An upper mantle diapir in the eastern Klamath Mountains, northern California. J. Geophys. Res., Geol. Soc. Am. Spec. Pap. 86, 11837.
Rampone, E., Borghini, G., 2008. Melt migration and intrusion in the Erro-Tobbio peridotites (Ligurian Alps, Italy): Insights on magmatic processes in extending lithospheric mantle. Eur. J. Mineral. 20, 573–585.
Raterron, P., Amiguet, E., Chen, J., Li, L., Cordier, P., 2009. Experimental deformation of olivine single crystals at mantle pressures and temperatures. Phys. Earth Planet. Inter. 172, 74–83.
Raterron, P., Chen, J., Geenen, T., Girard, J., 2011. Pressure effect on forsterite dislocation slip systems: Implications for upper-mantle LPO and low viscosity zone. Phys. Earth Planet. Inter. 188, 26–36.
Raterron, P., Chen, J., Li, L., Weidner, D., Cordier, P., 2007. Pressure-induced slip-system transition in forsterite: Single-crystal rheological properties at mantle pressure and temperature. Am. Mineral. 92, 1436–1445.
Raterron, P., Girard, J., Chen, J., 2012. Activities of olivine slip systems in the upper mantle. Phys. Earth Planet. Inter. 200–201, 105–112.
Ribe, N.M., Yu, Y., 1991. A theory for plastic deformation and textural evolution of olivine polycrystals. J. Geophys. Res. [Solid Earth] 96, 8325–8335.
Ringwood, A.E., 1975. Composition and Petrology of the Earth’s Mantle. McGraw-Hill.
Russell, J.B., Gaherty, J.B., Lin, P.P., Lizarralde, D., Collins, J.A., Hirth, G., Evans, R.L., 2019. High-Resolution Constraints on Pacific Upper Mantle Petrofabric Inferred From Surface-Wave Anisotropy. J. Geophys. Res. [Solid Earth] 124, 631–657.
Sachs, G.Z., 1928. The plastic deformation mode of polycrystals. Z. Ver. Dtsch. Ing. 72, 734.
Salters, V.J.M., Stracke, A., 2004. Composition of the depleted mantle. Geochem. Geophys. Geosyst., Geol. Soc. Spec. Publ. 5. https://doi.org/10.1029/2003GC000597
Schaeffer, A.J., Lebedev, S., 2013. Global shear speed structure of the upper mantle and transition zone. Geophys. J. Int. 194, 417–449.
Schaeffer, A.J., Lebedev, S., Becker, T.W., 2016. Azimuthal seismic anisotropy in the Earth’s upper mantle and the thickness of tectonic plates. Geophys. J. Int. 207, 901–933.
Schwindinger, K.R., Anderson, A.T., 1989. Synneusis of Kilauea Iki olivines. Contrib. Mineral. Petrol. 103, 187–198.
Signorelli, J., Tommasi, A., 2015. Modeling the effect of subgrain rotation recrystallization on the evolution of olivine crystal preferred orientations in simple shear. Earth Planet. Sci. Lett. 430,

356–366.
Silver, P.G., 1996. SEISMIC ANISOTROPY BENEATH THE CONTINENTS: Probing the Depths of Geology. Annual Review of Earth and Planetary Sciences. https://doi.org/10.1146/annurev.earth.24.1.385
Silver, P.G., Chan, W.W., 1988. Implications for continental structure and evolution from seismic anisotropy. Nature 335, 34–39.
Skemer, P., Hansen, L.N., 2016. Inferring mantle flow from seismic anisotropy: An experimental perspective. Tectonophysics 1–14.
Skemer, P., Warren, J.M., Hansen, L.N., Hirth, G., Kelemen, P.B., 2013. The influence of water and LPO on the initiation and evolution of mantle shear zones. Earth Planet. Sci. Lett. 375, 222–233.
Sleep, N.H., Warren, J.M., 2014. Effect of latent heat of freezing on crustal generation at low spreading rates. Geochemistry, Geophysics, Geosystems. https://doi.org/10.1002/2014gc005423
Spiegelman, M., Kelemen, P.B., Aharonov, E., 2001. Causes and consequences of flow organization during melt transport: The reaction infiltration instability in compactible media. J. Geophys. Res. [Solid Earth] 106, 2061–2077.
Sundberg, M., Cooper, R.F., 2008. Crystallographic preferred orientation produced by diffusional creep of harzburgite: Effects of chemical interactions among phases during plastic flow. J. Geophys. Res. 113, B12208.
Takazawa, E., Okayasu, T., Satoh, K., 2003. Geochemistry and origin of the basal lherzolites from the northern Oman ophiolite (northern Fizh block). Geochem. Geophys. Geosyst. 4.
Tanimoto, T., Anderson, D.L., 1984. Mapping convection in the mantle. Geophys. Res. Lett. 11, 287–290.
Tasaka, M., Zimmerman, M.E., Kohlstedt, D.L., Stünitz, H., Heilbronner, R., 2017. Rheological weakening of olivine+ orthopyroxene aggregates due to phase mixing: Part 2. Microstructural development. J. Geophys. Res. [Solid Earth] 122, 7597–7612.
Taylor, G.I., 1938. Plastic deformation of metals. 1. J. Inst. Met. 62, 307.
Tielke, J.A., Zimmerman, M.E., Kohlstedt, D.L., 2017. Hydrolytic weakening in olivine single crystals. J. Geophys. Res. [Solid Earth] 122, 2017JB014004.
Tielke, J.A., Zimmerman, M.E., Kohlstedt, D.L., 2016. Direct shear of olivine single crystals. Earth Planet. Sci. Lett. 455, 140–148.
Tommasi, A., 1998. Forward modeling of the development of seismic anisotropy in the upper mantle. Earth Planet. Sci. Lett. 160, 1–13.
Tommasi, A., Mainprice, D., Canova, G., Chastel, Y., 2000. Viscoplastic self-consistent and equilibrium-based modeling of olivine lattice preferred orientations: Implications for the upper mantle seismic anisotropy. J. Geophys. Res. 105, 7893–7908.
Tommasi, A., Tikoff, B., Vauchez, A., 1999. Upper mantle tectonics: three-dimensional deformation, olivine crystallographic fabrics and seismic properties. Earth Planet. Sci. Lett. 168, 173–186.
Tommasi, A., Vauchez, A., 2015. Heterogeneity and anisotropy in the lithospheric mantle. Tectonophysics. https://doi.org/10.1016/j.tecto.2015.07.026
Tommasi, A., Vauchez, A., 2001. Continental rifting parallel to ancient collisional belts: an effect of the mechanical anisotropy of the lithospheric mantle. Earth Planet. Sci. Lett. 185, 199–210.
Tommasi, A., Vauchez, A., Godard, M., Belley, F., 2006. Deformation and melt transport in a highly depleted peridotite massif from the Canadian Cordillera: Implications to seismic anisotropy above subduction zones. Earth Planet. Sci. Lett. 252, 245–259.
Vauchez, A., Tommasi, A., Barruol, G., Maumus, J., 2000. Upper mantle deformation and seismic anisotropy in continental rifts. Phys. Chem. Earth Part A. 25, 111–117.
Waff, H.S., Faul, U.H., 1992. Effects of crystalline anisotropy on fluid distribution in ultramafic partial melts. J. Geophys. Res. 97, 9003.
Warren, J.M., Hirth, G., Kelemen, P.B., 2008. Evolution of olivine lattice preferred orientation during simple shear in the mantle. Earth Planet. Sci. Lett. 272, 501–512.
Weatherley, S.M., Katz, R.F., 2012. Melting and channelized magmatic flow in chemically

heterogeneous, upwelling mantle. Geochemistry Geophysics Geosystems. https://doi.org/10.1029/2011gc003989
Webber, C., Newman, J., Holyoke, C.W., Little, T., Tikoff, B., 2010. Fabric development in cm-scale shear zones in ultramafic rocks, Red Hills, New Zealand. Tectonophysics 489, 55–75.
Wheeler, J., 2010. Anisotropic rheology during grain boundary diffusion creep and its relation to grain rotation, grain boundary sliding and superplasticity. Philos. Mag. 90, 2841–2864.
Wheeler, J., 09/2009. The preservation of seismic anisotropy in the Earth's mantle during diffusion creep. Geophys. J. Int. 178, 1723–1732.
Wolfe, C.J., Solomon, S.C., 1998. Shear-wave splitting and implications for mantle flow beneath the MELT region of the east pacific rise. Science 280, 1230–1232.
Workman, R.K., Hart, S.R., 2005. Major and trace element composition of the depleted MORB mantle (DMM). Earth Planet. Sci. Lett. 231, 53–72.
Yuan, H., Romanowicz, B., 2010. Lithospheric layering in the North American craton. Nature 466, 1063–1068.
Zhang, S., Karato, S.-I., 1995. Lattice preferred orientation of olivine aggregates deformed in simple shear. Nature 375, 774–777.
Zhang, S., Karato, S.-I., Fitz Gerald, J., Faul, U.H., Zhou, Y., 2000. Simple shear deformation of olivine aggregates. Tectonophysics 316, 133–152.
Zhong, X., Frehner, M., Kunze, K., Zappone, A., 2014. A novel EBSD-based finite-element wave propagation model for investigating seismic anisotropy: Application to Finero Peridotite, Ivrea-Verbano Zone, Northern Italy. Geophysical Research Letters. https://doi.org/10.1002/2014gl060490

Declaration of interests

 The authors declare that they have no known competing financial interests or personal relationships that could have appeared to influence the work reported in this paper.

The authors declare the following financial interests/personal relationships which may be considered as potential competing interests: